Theses, Dissertations and Culminating Projects

5-2018

Geochemical and Sedimentological Analysis of Marine Sediments from ODP Site 696 and Implications for the Onset of Antarctic Glaciation

Allison Paige Lepp
Montclair State University

Follow this and additional works at: https://digitalcommons.montclair.edu/etd

Part of the Environmental Sciences Commons

ABSTRACT

The Eocene-Oligocene Transition (EOT) approximately 34 million years ago (Ma) marks the shift from the warm greenhouse conditions of the Eocene to today's icehouse, and was accompanied by the establishment of the East and West Antarctic Ice Sheets. Details surrounding the timing, magnitude, and regional expansion of glaciation are poorly constrained primarily due to low core recovery and lack of reliable age models, and therefore warrant continued investigation. A recently updated age model applied to Ocean Drilling Program (ODP) Site 696, located in the northwest sector of the Weddell Sea, indicates Core 55R represents a high-recovery succession encompassing the EOT. This project presents a high-resolution, multimethod analysis of this sediment core.

Laser particle size analysis was performed throughout the core, and inductively coupled plasma mass spectrometry and optical emission spectrometry are used to quantify major, trace, and rare earth elemental concentrations on samples with >80% mud. Paleoclimate proxies are calculated to characterize the dominant weathering regime and degree of glacial influence on sediment. Results indicate a cool, dry climate and sediment with a strong glacial signature, as evidenced by low chemical index of alteration (CIA) values and significant contribution of glacial rock flour. Trace and REE ratios do not suggest major changes in source material, and felsic versus mafic plots indicate 55R sediment is felsic to intermediate in composition. Sediment remains well sorted throughout, and therefore elemental enrichments are likely related to grain-size partitioning.

Results of this study have implications for the investigation into continental glacial history of Antarctic through the EOT; 55R sediments reflect a similar climate to shelf sediments retrieved from Prydz Bay and Wilkes Land Margins and are consistent with significant terrestrial cooling across East Antarctica during the late Eocene. Studies from West Antarctica, however, suggest a later onset with less glacial stability. Similar high-resolution studies are thusly needed to further improve our understanding of Antarctic ice dynamics in response to climate perturbations.

MONTCLAIR STATE UNIVERSITY

Geochemical and Sedimentological Analysis of Marine Sediments from ODP Site 696
and Implications for the Onset of Antarctic Glaciation

by

Allison Lepp

A Master's Thesis Submitted to the Faculty of

Montclair State University

In Partial Fulfillment of the Requirements

for the Degree of
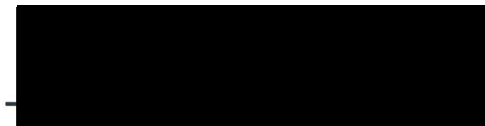
Master of Science

May 2018

College of Science and Mathematics

Department of Earth and
Environmental Studies

Thesis Committee:

Dr. Sandra Passchier
Thesis Sponsor

Dr. Stefanie Brachfeld
Committee Member
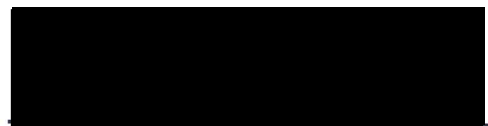
Dr. Xiaona Li
Committee Member

Geochemical and Sedimentological Analysis of Marine Sediments from ODP Site 696 and Implications for the Onset of Antarctic Glaciation

A THESIS

Submitted in partial fulfillment of the requirements

for the degree of Master of Science

by

ALLISON PAIGE LEPP

Montclair State University

Montclair, NJ

2018

ACKNOWLEDGEMENTS

TABLE OF CONTENTS

LIST OF FIGURES

LIST OF TABLES

1. INTRODUCTION

1.1 Background

The Eocene-Oligocene Transition (EOT) approximately 34 million years ago (Ma) signifies a global climactic shift from a warm greenhouse to the present-day icehouse. This shift was notably accompanied by a dramatic drop in global sea level (Stocchi et al., 2013), a decrease in atmospheric carbon dioxide concentration (Pearson et al., 2009; Pagani et al., 2005), reduction in terrestrial biodiversity and vegetation (Anderson et al., 2011; Francis et al., 2009), and the development of the modern-day Antarctic Ice Sheet (Coxall and Wilson, 2011). Recent literature agrees that the drivers behind this climate shift were the combination of an orbital geometry favoring cool summers and a decline in atmospheric CO_2 (e.g., Anderson et al., 2011, Coxall et al., 2005, Zachos et al., 2001); the result was abrupt global cooling that enabled the transition from an ice-free planet to continental-scale ice sheets on Antarctica to occur in less than 400,000 years (Coxall et al., 2005).

1.1.1 *Evidence of the EOT*

Perhaps the most compelling piece of evidence for significant global cooling at 34 Ma comes from dramatic excursions in deep-sea oxygen isotope records (Zachos et al., 2001). Such isotope archives are obtained through the analysis of benthic foraminifera, unicellular protists whose skeletal fragments are preserved in the sediment record and reflect the ocean chemistry at the time their shells were produced. Ocean water enriched in the heavy isotope ^{18}O implies a greater concentration of the lighter isotope, ^{16}O, is
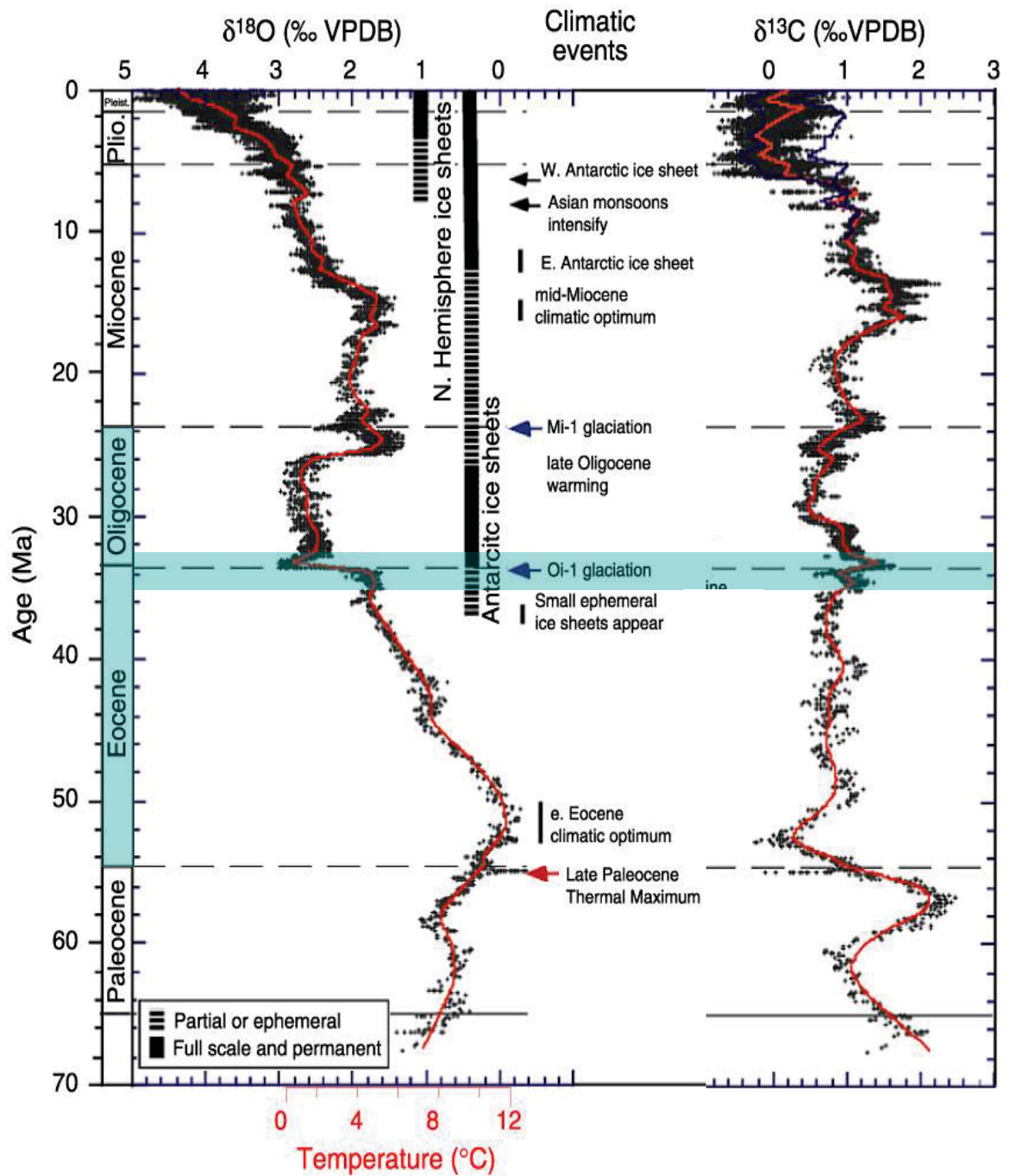
Figure 1: Global composite of $\delta^{18}O$ and $\delta^{13}C$ adapted from Zachos et al (2001). Prominent increase in $\delta^{18}O$ seen at 33.7 Ma is referred to Oi-1 isotope excursion. Legend indicates ephemeral glaciation beginning in the mid- to late-Eocene at ~37 Ma, and full-scale ice-sheets are present after 33.7 Ma.

preferentially stored on land as glacial ice. A global isotopic composite assembled by Zachos et al. (2001) that incorporates data from over 40 drill locations shows a steady increase in $\delta^{18}O$ following the early Eocene climactic optimum (~50 Ma), and a high magnitude spike at 33.7 Ma (Figure 1). This spike is referred to as the Oligocene isotope event, or Oi-1, and has been interpreted as marking the established presence of full scale, permanent ice sheets on the South Pole (Zachos et al., 2001). The absolute age of the Oi-1 event has since been improved from 33.7 Ma to 33.5 Ma (Vandenberghe et al., 2012).

The EOT is also characterized by a deepening of the ocean carbonate compensation depth (CCD). The CCD is the depth below which the seawater is undersaturated with respect to calcite, and therefore calcium carbonate minerals dissociate rather than accumulate (Misra, 2012). The CCD varies as a function of ocean temperature and acidity, and its signature in the sediment record can thusly reflect past atmospheric carbon concentrations and global climate (Coxall et al., 2005). Well-dated sediment records spanning the EOT from both mid- to high-latitudes and Pacific Ocean drill sites indicate a significant (>1km) deepening of the CCD as evidenced by increases in $CaCO_3$ mass accumulation rates. The appearance of carbonate deposits in low-latitude ocean basin sediments is temporally consistent with increases in $\delta^{18}O$ from all locations, confirming global-scale cooling during the EOT (Coxall et al., 2005).

The Oi-1 isotope excursion is concurrent with an observed regime shift in Southern Ocean plankton communities, and an increase in global ocean productivity (Houben et al., 2013; Zachos et al., 2001); this suggests an enhanced supply of nutrient-rich minerals to ocean waters via heightened glacial erosion and perhaps seasonal nutrient transport by sea-ice (Duprat et al., 2016; Houben et al., 2013). Additionally, observed

shifts in mid-latitude clay mineralogy (Wang et al., 2013) and paleoclimate

reconstructions that indicate low-latitude surface water cooling (Lear et al., 2008) support

the hypothesis that temperature decrease across the EOT was ubiquitous and not confined

to polar regions.

1.1.2 *Development of Antarctic Ice Sheets*

The growth of Antarctic glaciers across this transition is documented as occurring

in two steps, each lasting ~40 thousand years (kyr), with ~200 kyr between events

(Coxall et al., 2005). The first step, referred to as EOT-1, is characterized as "precursor"

glaciation in response to declining atmospheric CO_2 from the high (~1000-2000 ppmv)

concentrations of the Eocene (Miller et al., 2009; Pagani et al., 2005); EOT-1 cooling is

reflected in a slight (~0.6‰) positive $\delta^{18}O$ excursion at 33.8 Ma (Katz et al., 2008). The

second step is marked by the larger (~1‰) Oi-1 isotope excursion at 33.5 Ma, and

denotes the presence of an established continental-scale ice sheet with a smaller,

additional cooling component (Passchier et al., 2017; Coxall et al., 2005; Zachos et al.,

2001).

The breadth of details surrounding spatial ice development, sensitivity, and

atmospheric CO_2 threshold behavior that are still uncertain warrants continued

investigation into Antarctica's ice sheet dynamics during the EOT. Mid- to late-Eocene

glaciation is believed to have nucleated in the high elevations of the Gamburtsev

Mountains (Rose et al., 2013), the Transantarctic Mountains and Dronning Maud Land

regions of East Antarctica (DeConto and Pollard, 2003), and perhaps even mountainous
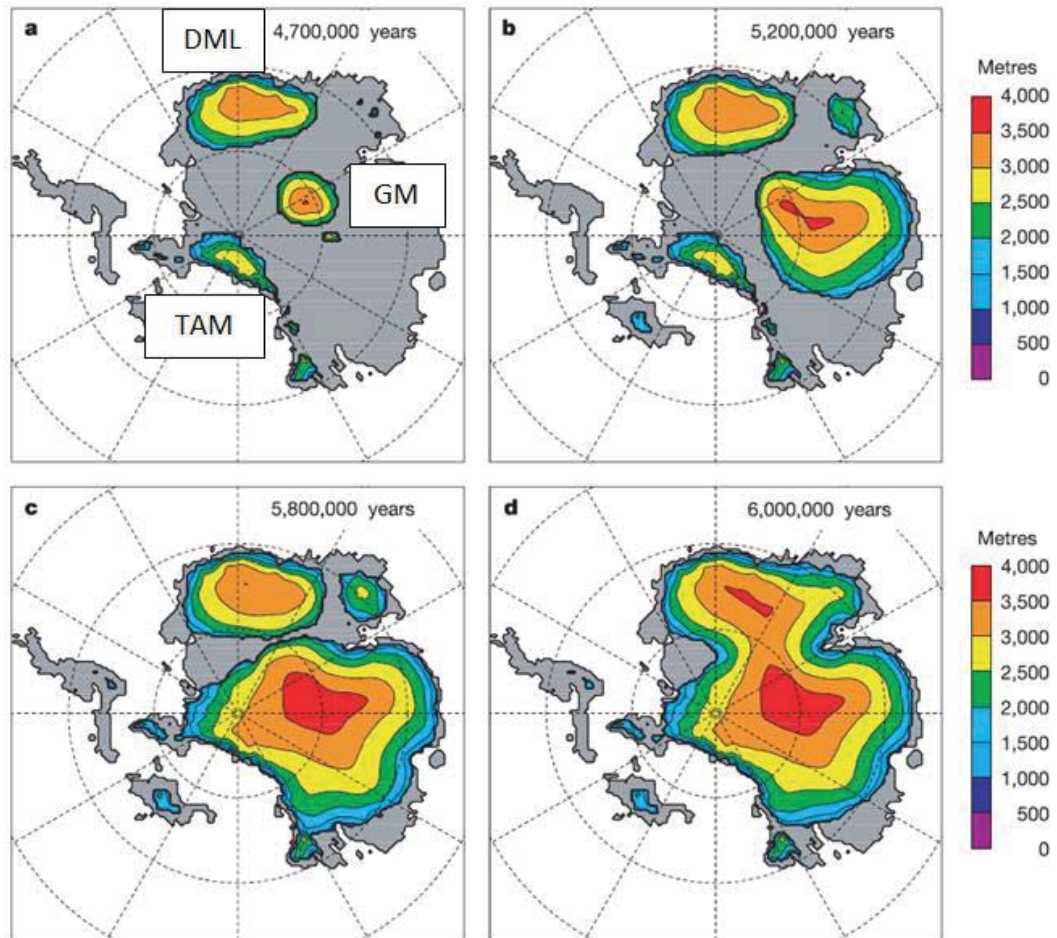
Figure 2: Results of combined global climate model and ice volume model from DeConto and Pollard (2003) depicting Antarctic ice development and expansion. Given ages are based on a 10 million year model run. Glaciation originates in areas of high (>3000m) elevation, and emanates to areas of lower relief. DML = Dronning Maud Land, TAM = Transantarctic Mountains, GM = Gamburtsev Subglacial Mountains.

regions of the Antarctic Peninsula (Anderson et al., 2011; Francis et al., 2008). The

progressive decline in atmospheric CO_2 (Pearson et al., 2009) in conjunction with cool

summers resulting from low eccentricity and obliquity geometries (Coxall et al., 2005)

enabled nascent cirque glaciers to coalesce, eventually forming the modern-day Antarctic

Ice Sheet (AIS; Figure 2). Recent records compiled from various continental margin sediment cores and geophysical surveys indicate that large-scale glaciation began on East Antarctica prior to the EOT-1 isotope excursion (e.g., Gulick et al., 2017, Passchier et al., 2017, Carter et al., 2016). However, additional records from the Ross Sea embayment of West Antarctica suggest marine-terminating ice did not stabilize until 32.8 Ma, well after the transition (Galeotti et al., 2016). Conflicting chronologies imply glacial expansion did not occur synchronously across the continent, and present a need to improve temporal constraints of ice development on East and West Antarctica.

Today, the relevance of this research is unequivocal: atmospheric CO_2 has exceeded a level (400 ppm) not seen since 3 Ma, human-induced warming of just 1°C was already accompanied by 20 cm of global sea level rise (SLR), and research predicts additional global SLR of 25-30 cm is inevitable over the next 40 years (Naish, 2017). AIS melting has the potential to significantly contribute to global SLR, and current satellite measurements show increased melting of Antarctic ice shelves in response to Southern Ocean warming (Naish, 2017). Models that can accurately project ice sheet collapse in response to various degrees of warming therefore have immediate implications for global policy and environmental protection initiatives. To advance understanding of ice-climate dynamics and improve models for future projections, it is imperative that research continues reconstructing past ice behavior from times of great climate variability. This project seeks to contribute to this objective through the multi-method analysis of well-dated, near-shore Antarctic sediments that span the EOT.

1.2 **Study Location**

1.2.1 *ODP Site 696*

Site 696 is one of nine sites drilled in the Weddell Sea region during Ocean Drilling Program (ODP) Leg 113 in 1987 (Shipboard Scientific Party, 1988). In addition to characterizing the evolution of planktonic productivity and exploring the initiation of cold Antarctic bottom water in the Weddell Sea sector, a primary objective of Leg 113 was to investigate the temporal development of the modern-day Antarctic ice sheet (Shipboard Scientific Party, 1988). Located on the southeast margin of the South Orkney Microcontinent (SOM), Site 696 is an ideal geographic location to examine Antarctica's glacial history in the Weddell Sea sector (Figure 3). Continental margin sediments provide an essentially undisturbed record of paleoenvironmental conditions such as changes in sediment supply, ocean geochemistry and temperature, and variations in regional sea level (Passchier et al., 2017; Galeotti et al., 2016). At the poles specifically, these marginal sediments are useful in reconstructing glacial advance and retreat cycles and preserving outsized clasts (e.g., Gulick et al., 2017, Carter et al., 2016).

Two holes, 696A and 696B, were drilled at 650 meters water depth. Only 12 cores were recovered from Hole A due to difficulties with the bottom hole assembly. Hole B was significantly more successful; 62 cores were recovered to a maximum depth of 645.6 mbsf (Shipboard Scientific Party, 1988). Shipboard scientists divided cores into lithostratigraphic units based primarily on smear slide analyses and observational maturity (Shipboard Scientific Party, 1988). Additional characteristics including clay mineralogy, seismic stratigraphy, and paleomagnetic assignments were observed and described in detail in the site report (Shipboard Scientific Party, 1988).
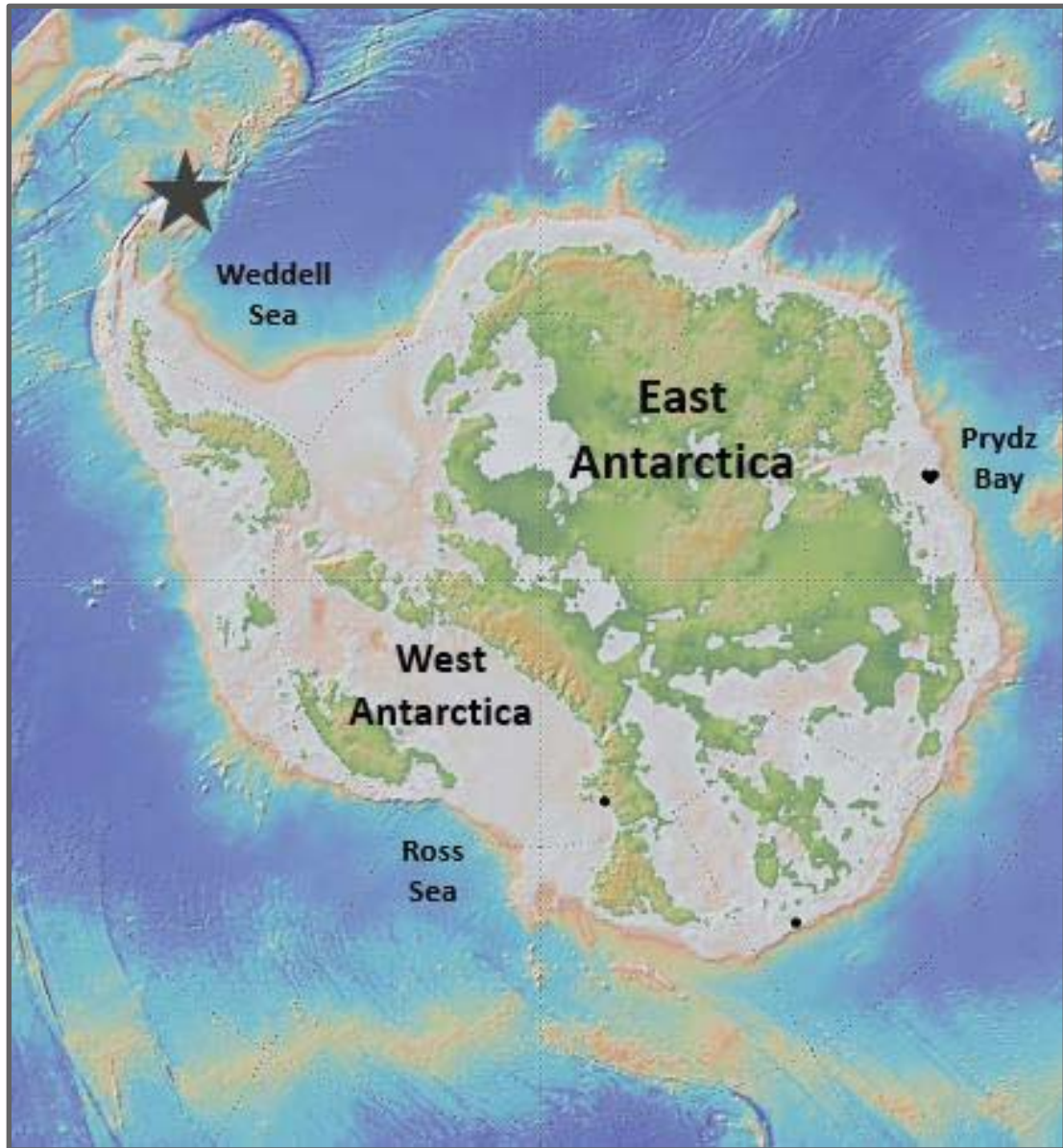
Figure 3: GeoMap App rendered map showing location of ODP Site 696 (star) in the northwestern Weddell Sea. Recent studies from drill sites in Prydz Bay, the Ross Sea, and Wilkes Land Margin that provide evidence for asynchronous East and West Antarctic ice sheet expansion across the E-O transition are also noted (dots).

1.2.2 *Weddell Sea Sector Tectonics and Geology*

The continent of Antarctica has a rich and complex tectonic history dating back to the inception of the East Antarctic craton in the Early Archean (Anderson,1999). While major geologic development of East Antarctica was complete by the early Paleozoic (Anderson, 1999), West Antarctica's tectonic history is more recent and complex. West Antarctica is comprised of five continental blocks (Marie Byrd Land, Thurston Island, Antarctic Peninsula, Haag Nunataks, and Ellsworth-Whitmore Mountains) that formed amidst the breakup of Gondwanaland during the Mesozoic era (Lee et al., 2012; Fitzgerald, 2002). These microplates continued to rotate and translate until reaching their present configuration approximately 110 Ma (Fitzgerald, 2002). It was this tectonically-driven rotation that allowed for the opening of the Weddell Sea c. 165 Ma (Fitzgerald, 2002).

Tectonic activity continued to affect West Antarctica through the mid-Cenozoic; during the late-Eocene, rifting separated the South American plate and Antarctic Peninsula microplate, opening the Drake Passage and forming the South Scotia Ridge (Busetti et al., 2000). It is likely this event separated the SOM from the northern tip of the Antarctica Peninsula (Eagles and Livermore, 2002); regional extension continued from ~37 to 23 Ma (Eagles and Livermore, 2002), opening the Powell Basin c. 29 Ma and geographically isolating the SOM (Figure 4). Paleomagnetic reconstructions indicate during the EOT, sedimentation on the shelf of the SOM would have been restricted to local sources of the Antarctic Peninsula, or ice-rafted debris (IRD) from distal formations (Eagles and Livermore, 2002; Busetti et al., 2000).
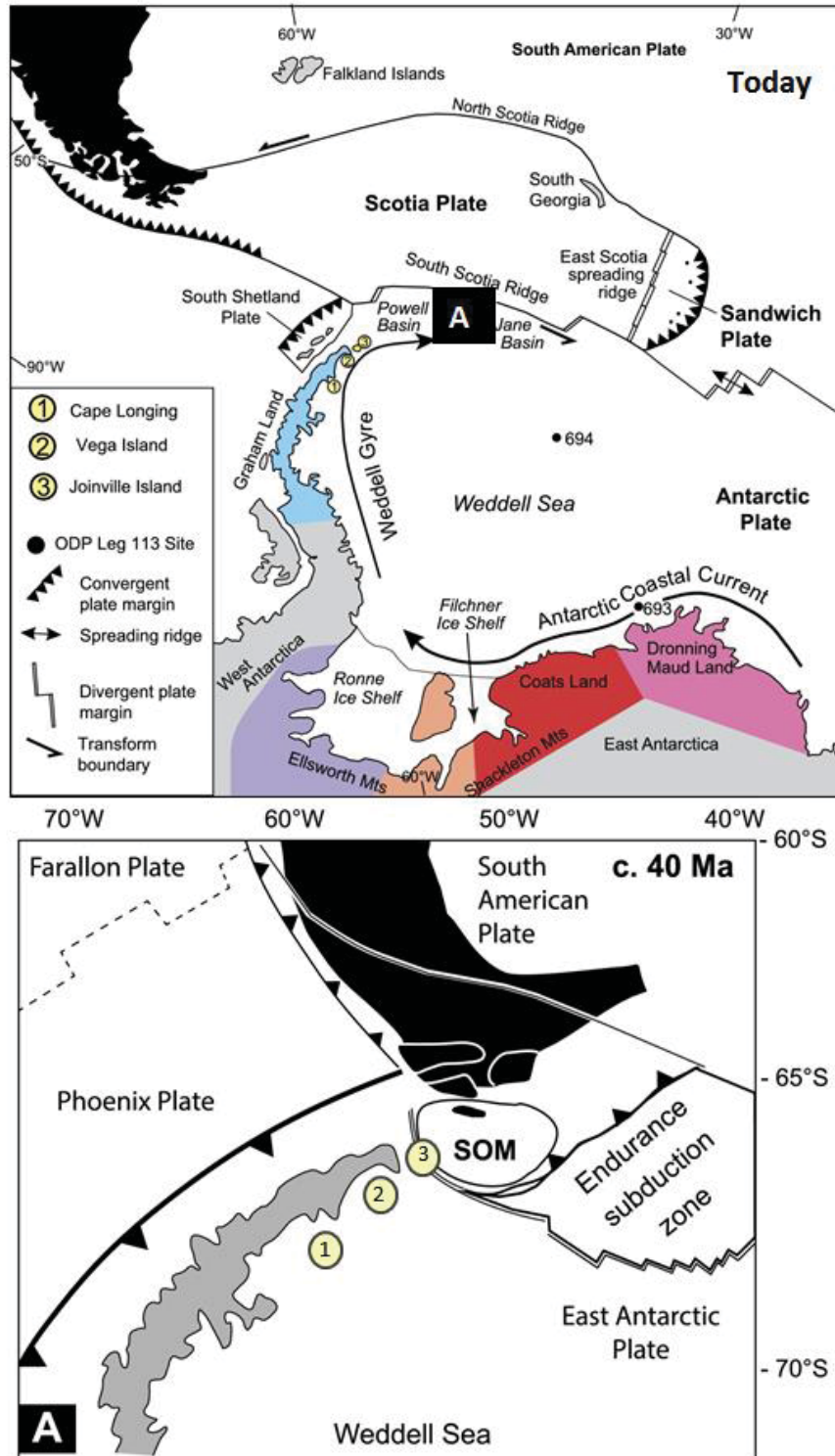
Figure 4: Weddell Sea regional tectonics and translation of the SOM from the northern tip of the Antarctic Peninsula ~40 Ma to its present-day location. Adapted from Carter et al. (2016).

The Weddell Sea basin is a unique depositional setting in that it receives terrigenous detrital material from both East and West Antarctic formations (Figure 5). Its eastern border is formed by Dronning Maud Land (DML), consisting of granodioritic migmatites, amphibolite gneiss facies, and boasting elevations in excess of 3000 m (Paulsson and Austrheim, 2003). Moving westward, the southern boundary of the Weddell Sea is defined by the mafic gneisses and metagranitoids of East Antarctica's Shackleton Range, and predominantly granites and granodiorites of West Antarctica's
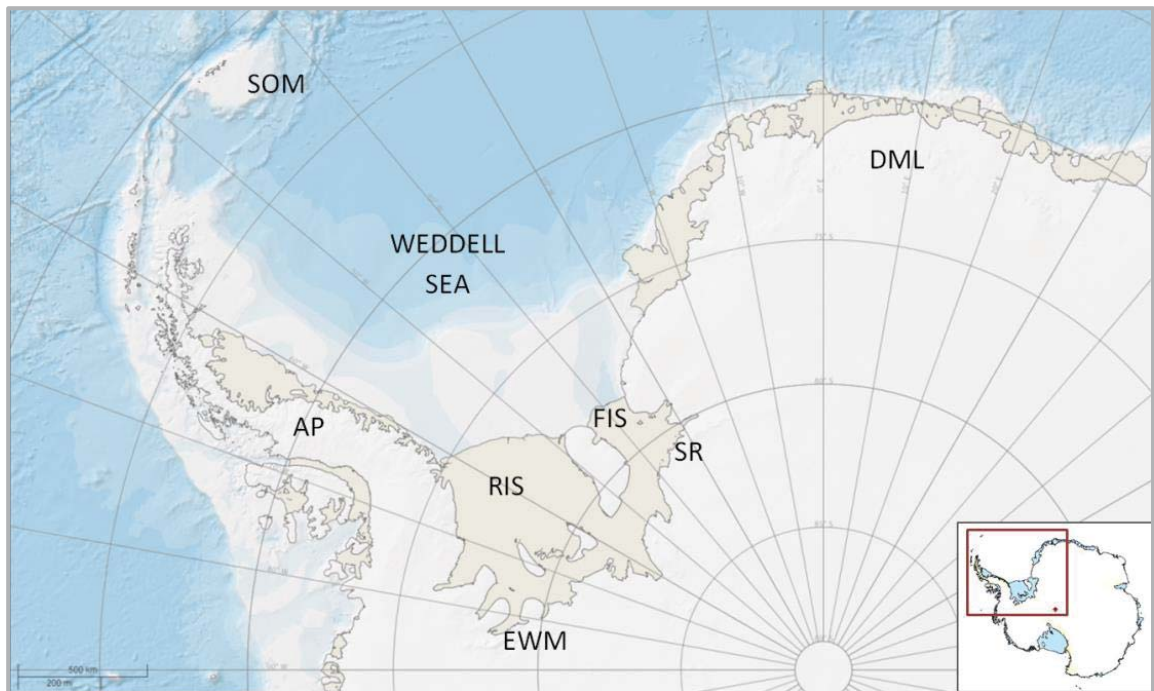
Figure 5: Weddell Sea sector formations. AP = Antarctic Peninsula. EWM = Ellsworth-Whitmore Mountains. SR = Shackleton Range. DML = Dronning Maud Land. SOM = South Orkney Microcontinent. Also labeled are present-day ice shelves, RIS = Ronne Ice Shelf and FIS = Filchner Ice Shelf. Map generated using the online Antarctic Digital Database Map Viewer from SCAR.

Ellsworth-Whitmore Mountains (Will et al., 2010; Vennum and Storey, 1987). These two

regions are geographically separated by the 3500-km long Transantarctic Mountain

(TAM) range (Fitzgerald, 2002), which may also supply lithogenic material to the

Weddell Sea basin. The western border of the Weddell Sea is defined by the Antarctic

Peninsula, which is comprised of upper-Paleozoic to lower-Mesozoic sandstones and

mudstones in the north (Castillo et al., 2014), and both calc-alkaline volcanic rocks and

back-arc basin sedimentary sequences in the south (Vennum and Rowley, 1986).

1.3 **Age Model**

Much of the ambiguity through the EOT can be attributed to poor core recovery

and lack of certainty in assigning core ages (Houben et al., 2013; Coxall et al., 2005). The

shipboard sequence dating of cores from Site 696 involved bio- and

magnetrostratigraphic methods (Shipboard Scientific Party, 1988). However, poor

preservation of radiolarian and other stratigraphically useful microfossils from much of

the lower (i.e., from ~530 to 645.6 mbsf) cores meant age constraints through the

Paleogene had potential for error.

A recent (2013) study investigated dinoflagellate fossil assemblages in several

cores from the Antarctic margin in order to identify cooling-induced shifts in taxa, and

update existing core ages based on first and last occurrences (Houben et al., 2013).

Researchers examined Hole 696B and were able to improve age constraints by

identifying specific dinocyst appearances and calibrating with well-dated appearances

from other drill sites (Houben et al., 2013, *Supplementary Materials [SM]*). The study

identified the first occurrence (FO) of *Malvinia escutiana*, a marker taxon whose FO in a

South Atlantic drill core was correlated to the Oi-1 event (Houben et al., 2011), in Core

55R at 569.11 mbsf; this depth was thus assigned an age of 33.6 Myr (Houben et al., 2013, *SM*). Additionally, the FO of dinocyst *Stoveracysta kakanuiensis,* dated to 34.1 Myr, was observed in Core 55R at 571.55 mbsf (Houben et al., 2013, *SM*).

Using these age-to-depth correlations, an age model was constructed for the lower cores (55R-62R) of 696B (Figure 6). By combining the two relationships detailed above with a third FO of the calcareous nanofossil *Isthmolithus recurves* at 616.78 mbsf and dated to 36.27 Ma (Houben et al., 2013, *SM*), intermediate sample ages and linear sedimentation rates were calculated. The stratigraphic placement of *S. kakanuiensis* below *M. escutiana* indicates Core 55R, spanning from 568.7 to 576.1 mbsf, is a high-recovery core from a sedimentary succession that encompasses the complete EOT at 34 Ma (Figure 7). This study presents a high-resolution analysis of this core, incorporating geochemical and sedimentological methods, to determine the extent of glacial influence on sediment deposited at Site 696 across the EOT.

2. METHODOLOGY

2.1 Sedimentological Analysis

The initial analytical method used in this study was laser particle size analysis. The distribution of particle sizes within a sedimentary sample gives great insight to the environment during deposition, and any changes to that depositional environment, such as a new sediment source, shift in weathering regime, or variation in water depth are often reflected in grain size distribution (e.g., Passchier et al., 2017, Storti and Balsamo, 2010). From October 2016 to February 2017, laser particle size analysis was performed

55R Age Model
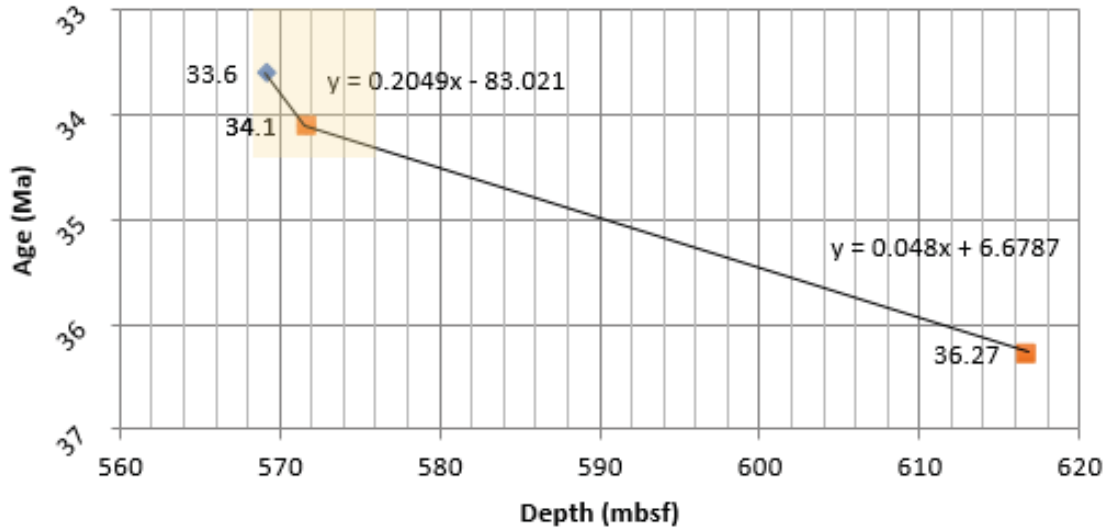
Figure 6: age model constructed for Core 55R using FO data for three taxa published by Houben et al. (2013). Equations represent linear sedimentation rates as calculated by Excel. Note the decrease in sedimentation rate following the FO of dinocyst *S. kakanuiensis* at 34.1 Ma. Shaded region represents 55R ages and depths.
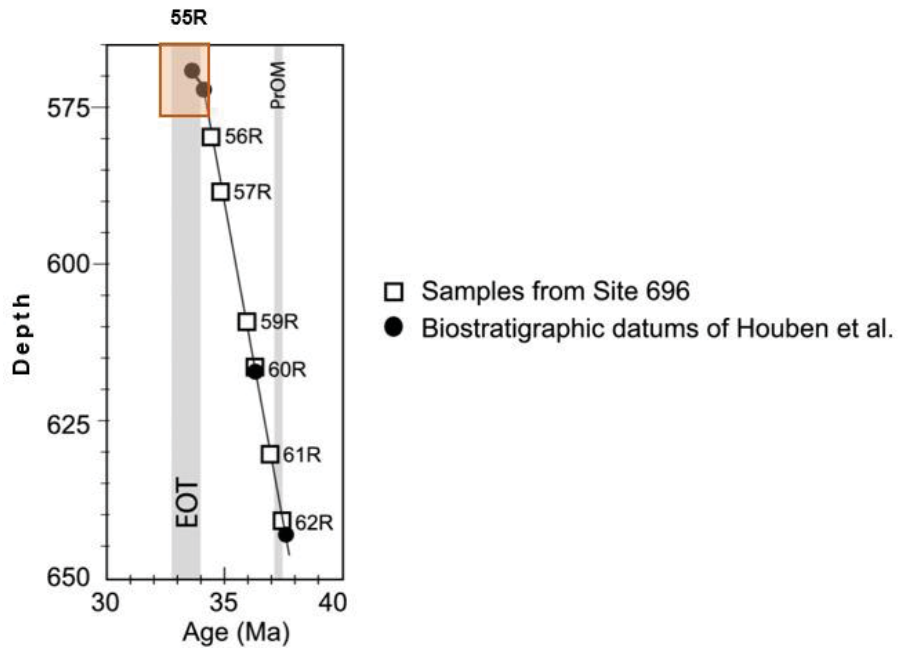
Figure 7: Depths (mbsf) and ages encompassed by 55R as obtained from age model in relation to downhole cores from 696B. PrOM = Preabonian oxygen isotope maximum. Image adapted from Carter et al. (2016).

on 75 samples from Sections 1-5 of Core 55R using the Malvern Mastersizer 2000 at Montclair State University.

2.1.1 *Sample selection*

The first step in determining which samples to examine involved applying the age model to sections 1-5 of Core 55R. Doing so yielded a maximum age of 34.3 Ma at a corresponding depth of 575.65 mbsf, and a minimum age of 33.52 Ma at corresponding depth 568.7 mbsf. Each section is divided into samples of two- to three-centimeter intervals; ages for individual samples were assigned by interpolating between the known datum published by Houben et al. (2013). As is reflected in the age model for 55R (Figure 6), the rate of deposition at Site 696 decreased after approximately 34.1 Ma, above corresponding depth of 571.6 mbsf. This shift is aligned with sample 40-42 cm of section 55R3. From this depth to the base of 55R5, the time between each sample was calculated as 2.4 kyr. Above this depth to the top of Core 55R, time between samples increases to 10.25 kyr.

The samples chosen for analysis were selected with an average of 10 kyr spacing to ensure sedimentation responses to obliquity and eccentricity cycles could be observed. Thus, in order to maintain a consistent spacing, this study analyzed every sample from 568.7 mbsf to the top of the core (49 total), and every fourth sample from 568.7 mbsf to the base of section 5 (26 total). Core sections with corresponding depths and ages are shown in Figure 8, and a complete listing of all samples is given in the appendix (Table A.1).

Core 55R
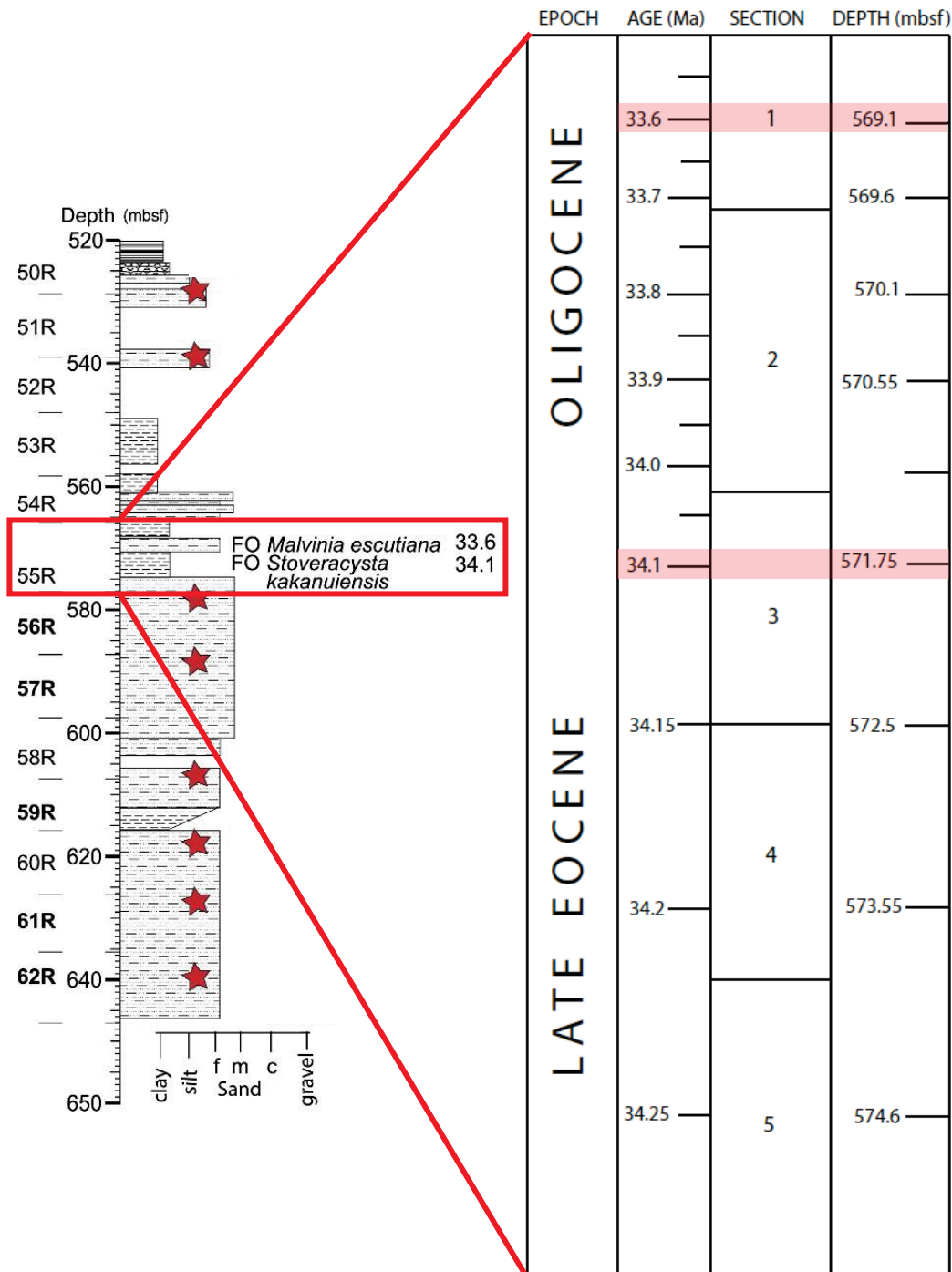
Figure 8: Lithologic log of lower cores from Site 696 (adapted from Carter et al., 2016). Core 55R is expanded to show sections used in this study with corresponding depths and ages as calculated from the age model. Shaded regions in 55R denote depths of dinocyst FOs that constrain the EOT. Stars indicate sample depths studied by Carter et al. (2016).

2.1.2 Sample preparation

Samples were prepared according to Konert and Vandenberghe (1997). Laser particle size analysis is restricted to grains less than 2mm in diameter; typically, samples are sieved to remove coarse-grained material. None of the samples used in this study, however, exhibited grains in excess of 2mm and therefore no sieving was required. Approximately 2-3 grams of sample were needed; for those samples with little cementation, it was possible to manually separate a representative subsample. For others, subsamples were separated with a hammer, and further disaggregated with a mortar and pestle using exclusively vertical pressure to avoid breaking grains. Each subsample was then placed in a 250-mL beaker and ~10 mL of 30% hydrogen peroxide was added to digest organic material. Millipore water was added to bring total volume to ~50 mL, and solutions were swirled and left to disaggregate completely. Beakers were then transferred to hot plates to encourage reactions. None of the samples from 55R reacted with H_2O_2. 2 mL of 10% HCl was then pipetted into each beaker to remove any carbonate content. Again, little to no reaction occurred in 55R samples. The solution was then allowed to boil off until total volume was <50 mL.

The beakers were removed from heat and cooled before components were transferred to labeled 50 mL polypropylene vials. The vials were transferred to a centrifuge and spun at 2000 rpm for 30 minutes. The supernatant was discarded, vials were refilled to 50 mL with Millipore water and shaken to resuspend sediment before another 30-minute centrifuge. After a second decantation, each specimen was returned to its original beaker and approximately half a teaspoon of sodium pyrophosphate, a dispersing agent, was added. Enough Millipore water to bring the solution to 50 mL was

added, and beakers were heated just long enough to dissolve the sodium pyrophosphate.

Finally, samples received at least 15 minutes of sonication. Samples that did not

disaggregate after 15 minutes received additional sonic baths in 15-minute intervals until

grains were sufficiently separated for analysis (Table A.2).

Four particularly resistant samples were prepared following the above procedure

but given a sodium hydroxide bath to further encourage disaggregation following

decantation. After the second decantation, vials were filled to 20 mL with Millipore

water, and 5 mL of NaOH was added before placing vials in a water bath between 85-

90ºC for one hour. Vials were then cooled, filled to 50 mL with Millipore water, and run

through the centrifuge at 2000 RMP for another 30 minutes. Following decantation and

two rounds of sonication, both 55R1 90-93 and 55R2 145-147 retained a single clump.

The clumps were manually removed, standard preparation was completed, and particle

size analysis was run with no further complications. A complete list of samples that

received modified preparation for laser particle size analysis is provided in the appendix

(Table A.2).

2.1.3 *Data acquisition and processing*

Data was collected using the Malvern Mastersizer 2000. The instrument projects

red and blue lasers through a glass cell while a centrifugal pump recirculates sample

suspended in Millipore water (Storti and Balsamo, 2010). Fifty-two sensors measure the

angles of light diffracted by the suspended sediments; the instrument then determines

grain size distribution based on the principle that the angle at which particles diffract light

increases logarithmically as particle size decreases (Storti and Balsamo, 2010). The

instrument was run using the standard operation procedure settings for fine-grained

sediments outlined by Sperazza et al. (2004) with a rotor speed of 2000 rpm. A stable background reading of ~650 mL Millipore water in an 800-mL beaker was used to measure the background prior to addition of each sample. After the background was measured, the sample was added to the beaker and the data collection began. Between samples, clean Millipore water was flushed through the instrument to avoid contamination, and the probe was thoroughly rinsed of residual sediment. Each sample was discarded after testing.

Results were exported into an Excel spreadsheet, and grain size percentages were compiled based on the following classification: grains between .02 and 3.9 microns as clay, grains between 3.9 and 62.5 microns as silt, and grains between 62.5 and 2000 microns as sand (Wentworth, 1922). The contribution from each of the three size classes was then calculated in Excel based on total volume within each sample.

2.2 **Geochemical Analysis**

To supplement sedimentological analysis outlined above, this study also incorporates examination of bulk geochemistry of samples to further understand paleoclimate conditions prior to and during deposition, as well as investigate potential sediment sources. Inductively-coupled plasma mass-spectrometry (ICP-MS) was performed using a ThermoFischer Scientific iCap-Q instrument at Montclair State University. A total of four runs was performed to obtain concentrations of trace and rare earth elements (REE). Inductively-coupled plasma optical emission spectrometry (ICP-OES) was conducted using a Horiba Jobin-Yvon Ultima instrument for three total runs to procure major element data.

2.2.1 *Sample selection*

Of the 75 samples analyzed for particle size distribution, 28 samples with mud fractions (<63µm) in excess of 80% were chosen for geochemical analysis via ICP-MS and ICP-OES. Samples were selected with a conscious effort to holistically represent sections 1-5 of Core 55R, with an emphasis on samples surrounding potentially transitionary deposits as interpreted through particle size data.

2.2.2 *Sample preparation*

28 samples were ground into a fine, homogenous powder with a mortar and pestle. Each sample was then weighed to 0.1000g +/- 0.0005g and mixed with 0.4000g +/- 0.002g of lithium metaborate flux on a weighing paper until homogenous. Weights of both sample and flux were recorded, and powdered mixtures were transferred to graphite crucibles. Crucibles were placed into a furnace at 1050º C for 30 minutes, creating a glass bead. During this time, 50 mL of 7% nitric acid and a magnetic stirbar were added to Teflon beakers. Once the crucibles were removed from the oven, each bead was immediately swirled and transferred to a beaker for complete acid digestion. Beakers were individually placed on a stirring plate to aid the bead's dissolution; once each bead was completely dissolved, the solution was funneled through filter paper into a 60 mL Nalgene bottle. This sample preparation was carried out according to Murray et al. (2000) and yielded master solutions with a 500x dilution factor.

Murray et al. (2000) recommend a 4000x dilution factor for analysis on the ICP-OES. This solution was created by pipetting 6.5 mL of the 500x master solution into new 60 mL Nalgene bottles. Then, 50 mL of 2% nitric acid was measured with a volumetric

flask and poured into the bottle. These 4000x solutions were stored in a refrigerator until ready for analysis. Instrumental sensitivity of ICP-MS makes it an ideal method for measuring trace and REE in bulk rock samples (Tamura et al., 2015); samples therefore required further dilution to 10,000x prior to ICP-MS analysis. This was done by pipetting 0.5 mL of each master solution into a test tube, and then adding 9.5 mL of 2% nitric acid for an additional dilution factor of 20x.

2.2.3 *Data acquisition and processing*

ICP-MS

Test tubes containing 10,000x diluted samples were racked and entered by sample ID according to rack placement into the iCap-Q software. The rack also included three blanks of only lithium metaborate flux and 12 United States Geological Survey (USGS) standards, prepared and diluted identical to samples. The instrument collected readings of a drift solution after every fourth sample; raw data was then exported into an Excel spreadsheet, and corrected for instrument drift and blank measurements. Ten of the 12 USGS standards with igneous compositions were used to derive calibration lines for each element. To assess accuracy of these calibrations, two sedimentary USGS rock powders were used as secondary standards.

A complete sample analysis consists of three runs; an initial run was conducted in July 2017, but technical difficulties with the instrument prevented completion of the final two runs. From this first run, exported data revealed precise calibrations for all minor elements. In October 2017, a new set of dilutions from the master solutions was prepared and three runs were successfully completed. Calibrations for rare earth and trace elements

were precise with the exception of Co. Data from all four runs was averaged and used in geochemical analysis, except Co, where only data procured during the initial run is used. Average trace and REE concentrations used in analysis are given in Tables A.3 and A.4, respectively.

ICP-OES

Samples were transferred from the 4000x dilution bottles into racked test tubes, whose corresponding sample IDs were input to the instrument software according to rack placement. Included in the rack were three blank solutions and 12 USGS standards, also with a dilution factor of 4000x, and drift measurements were taken after every fourth sample. Data processing in Excel revealed major element calibrations against USGS standards were precise in all three runs, except for element Mn for standard QLO-1. The calibration plot exhibited one outlying data point for the QLO-1 standard, which was removed from averages. Averaged major element concentrations are provided in Table A.5.

2.3 Paleoenvironmental Proxies and Ratios

2.3.1. *Ice-Rafted Debris Mass Accumulation Rate*

Major element results from the ICP-OES, in conjunction with particle size data, have been used to calculate the ice-rafted debris mass accumulation rate (IRD MAR). Fluctuations in IRD MAR can be indicative of both a change in a depositional environment's energy, and/or a shift in the supply of sediment to a sink. IRD MAR can also serve as a proxy to gauge sea-ice abundance (Hebbeln, 2000). Values were

calculated using the following equation from Krissek (1998):

$$IRD\ MAR\ (g/cm^2/kyr) = IRD\ \cdot LSR\ \cdot DBD\ \cdot TERR \qquad (1)$$

where IRD is the volume fraction of grains >125 microns (determined from laser particle

size data), LSR is the linear sedimentation rate (cm/kyr; obtained from the 55R age

model, Figure 6), DBD is the dry bulk density (g/cm^3), and TERR is the terrigenous

fraction. DBD was calculated according to Grützner (2003) using wet bulk density

obtained from the JANUS database (2017). The terrigenous fraction is given by:

$$TERR = 1 - (carbonate\ \% + biogenic\ silica\ \%) \qquad (2)$$

The carbonate percent was determined to be negligible on the grounds that (i) samples

exhibited little to no reaction to hydrochloric acid during particle size analysis

preparation and (ii) the smear slide analysis included in the Site 696 core report indicates

carbonate is absent in 55R (Shipboard Scientific Party, 1988). The biogenic silica percent

was calculated as excess silica according to Böning et al. (2005), where:

$$SiO_{2\ excess}\% = SiO_{2\ sample}\% - \left[\frac{SiO_{2\ lithogenic}}{Al_2O_{3\ lithogenic}} * Al_2O_{3\ sample}\%\right] \qquad (3)$$

Oxide sample percents were taken from ICP-OES data, and the lithogenic fraction was obtained from averaging published geochemical data from mudstones of the Hope Bay and Cape Legoupil Formations of the local Trinity Peninsula Group (Castillo et al., 2014, *SM*).

2.3.2. *Chemical Index of Alteration*

Major element data were also used to calculate the chemical index of alteration (CIA). CIA is a weathering proxy useful for differentiating between chemical and physical weathering regimes by examining the molar ratio of mobile cations commonly released in warm environments, and is calculated according to Nesbitt and Young (1982) as:

$$CIA = \frac{Al_2O_3}{Al_2O_3 + Na_2O + K_2O + CaO} \cdot 100 \qquad (4)$$

The calculations use molar weights of each oxide as determined from the normalized weight percents.

2.3.3 *Elemental Enrichments*

Interpreting trends and patterns in trace, rare earth, and major element concentration throughout the core is another analytical approach to better understand terrestrial weathering regimes and the nature of sediment origin. To begin, trace and rare earth elemental averages in ppm were calculated for each sample including data from all four ICP-MS runs. Those averages were then normalized to canonical values of the Upper Continental Crust (UCC) and average chondrite values for trace and REE,

respectively (McLennan, 2001; Nakamura, 1974). Results are displayed on logarithmic scales to better accentuate interesting geochemical deviations.

2.3.4 *Provenance Constraints*

The ability to correlate geochemical data to potential source rocks has implications for reconstructing ice growth in the Weddell Sea sector. To do so, this study analyzes fluctuations, ratios, and trends in trace and REE to observe possible changes in source material. Additionally, differentiating between felsic and mafic source rocks and evaluating agreement between samples and a variety of Antarctic formations will shed light on the regional glacial expansion within the Weddell Sea sector during the EOT.

To determine if sediment originated from one or several sources, a plot showing Al_2O_3 vs. TiO_2 and Sc vs. TiO_2 was constructed. Concentrations of these major and trace elements are not significantly altered by processes like weathering, sediment sorting, or diagenesis, and are therefore useful in provenance studies (Sheldon and Tabor, 2009; McLennan, 2001). Fluctuations in these ratios throughout the core would suggest multiple sources. Th/Sc was plotted against Zr/Cr to characterize the felsic-mafic nature of 55R sediments. Standards from USGS samples, the North American Shale Composite (NASC), and Mid-Ocean Ridge Basalt (MORB) were included for reference.

To further examine the origin of core sediments, a Th/U vs. Th plot (McLennan eta l., 1993) was made to compare 55R data with different crust/mantle sources and tectonic settings. Finally, 55R data were plotted with published averages from formations in the Weddell Sea sector of Antarctica, including the northern and southern Antarctic

Peninsula, Dronning Maud Land, the Shackleton Range, and Ellsworth-Whitmore Mountains, to evaluate geochemical similarities.

3. RESULTS

3.1 Particle Size Distributions

Laser particle size analysis shows that the sediments sampled in sections 1-5 of Core 55R are consistently dominated by silt, and contributing volume percent of clay and sand fluctuate (Figure 9). While distributions of individual samples exhibit greater variance, comparing the averages of each section yield clay percents ranging from 15.9 and 19.9, silt percents between 62.1 and 70.0, and sand percents between 10.0 and 20.4. There is an overall trend of increasing silt contribution upcore; this becomes evident when samples are plotted by section on a ternary diagram (Figure 10). The ternary projection also highlights individual samples whose sand contributions reach 40-50%. Additionally, the average volume contribution from clay-sized particles in 55R decreases slightly upcore.

Grain size distributions of individual samples are shown by section in Figure 11 accompanied by their average percent sand, silt, and clay. Here, the slight trend of increasing silt percent and decreasing clay percent upcore becomes more apparent. Each section can be characterized as exhibiting several bi-modal distributions that fall within the silt-sized range, with lesser and roughly equal contributions from clay and sand sized grains. Interestingly, each section except 55R3 exhibits at least one sample whose distribution is dominated by silt, but features a small, coarse-grained "tail"; this
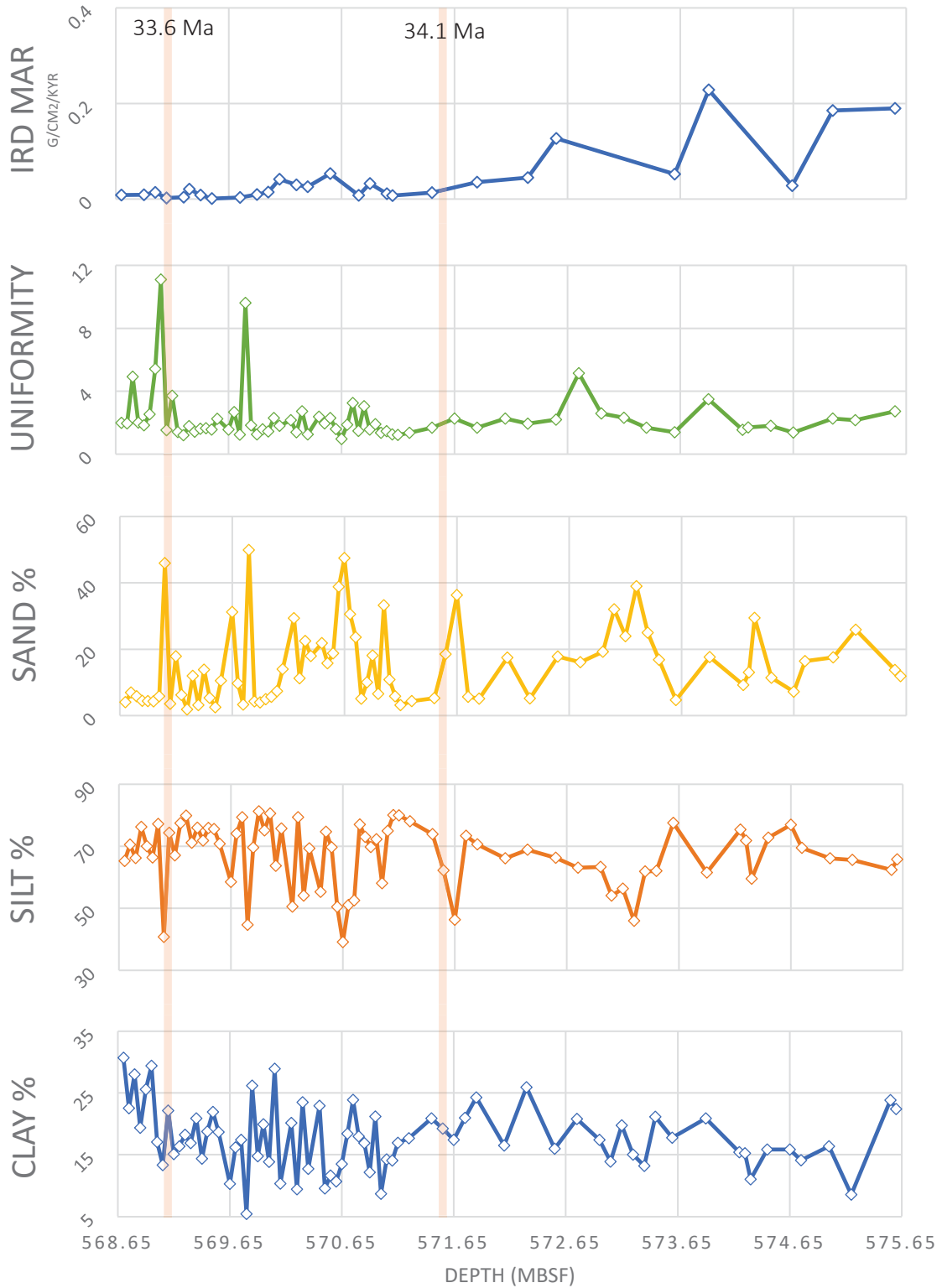
Figure 9: Results of particle size analysis for Core 55R. Clay, silt, and sand volume percents calculated according to the Udden-Wentworth classification scale, and age-tie points are included for reference. Also shown are plots of grain uniformity and IRD MAR. All values are plotted against core depth (mbsf).

distribution can be characteristic of fine (<2000 μm) ice-rafted debris (Hebbeln, 2000).

The earliest appearance of this distribution occurs at ~34.28 Ma.

Grain uniformity is also plotted alongside whole-core grain size distributions in

Figure 9. This property, calculated as D60/D10, or the diameter greater than that of 60%

of particles divided by the diameter greater than that of 10% of particles, is a quantitative

indicator of grain sorting (Passchier et al., 2018). Uniformity values of 4 or greater

denote poorly sorted sediment, and therefore may indicate increased glacial influence on
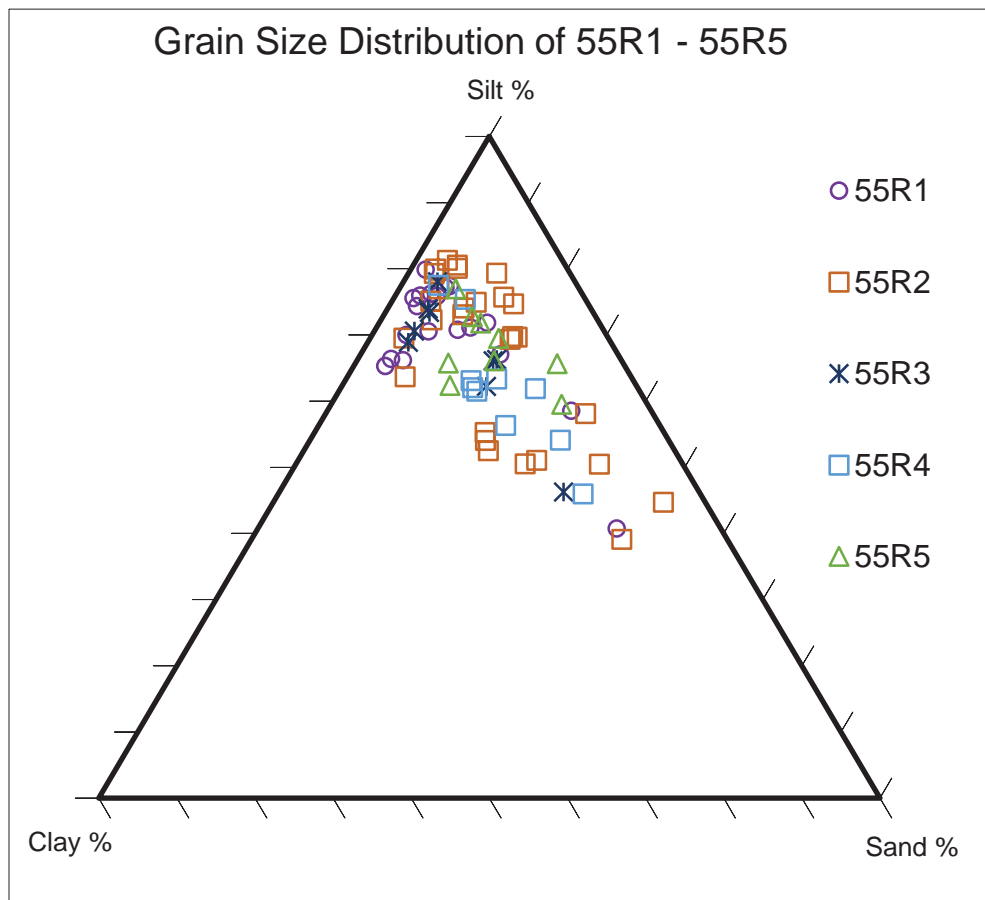
Figure 10. Ternary diagram showing particle size distributions of Core 55R by section. Silt dominates in vast majority of samples, while clay and sand percents fluctuate throughout the core.

Figure 11. a) through e) show particle size distributions of Core 55R plotted logarithmically by section. Silt fraction (4-63 microns) is shaded in each graph, and accompanying pie charts emphasize dominant silt contribution in each section.

sediment erosion. Below 572.75 mbsf (34.17 Ma), sediment remains well-sorted with an average uniformity value of 2.1, despite fluctuations in clay and sand percents. Upcore grain uniformity then begins to exhibit greater variation, and the two most significant peaks with values U>8 align with increases in sand percent above 569.8 mbsf (33.74 Ma).

3.2 **Geochemistry**

3.2.1 *Paleoenvironmental Proxies*

IRD MAR was calculated according to Equation 1, and combines both sedimentological and geochemical data to help characterize paleoenvironment. Results were plotted with units of $g/cm^2/kyr$ against core depth (Figure 9). Prior to ~34.14 Ma (572.3 mbsf), IRD MAR fluctuates between values as high as 0.22 and as low as 0.02 $g/cm^2/kyr$. Upcore, IRD MAR remains comparatively low, with values of 0.05 $g/cm^2/kyr$ or below. As noted in the equation, the linear sedimentation rate is factored into the calculation. Prior to 34.1 Ma, LSR is 2.025 cm/kyr. Sedimentation then drops over 75% to 0.491 cm/kyr. Figure 12 shows IRD MAR plotted against IRD, another variable in the calculation. The relationship seen here suggests IRD MAR values are significantly influenced by the differences in LSR, as numerous samples upcore of the sedimentation shift display comparable contributions from grains >125 µm. Values for DBD and TERR do not exhibit notable variation throughout 55R.

The CIA was calculated according to Equation 4 and plotted against core depth (Figure 13). Values remain below 65 throughout and show a core average of 61. Two
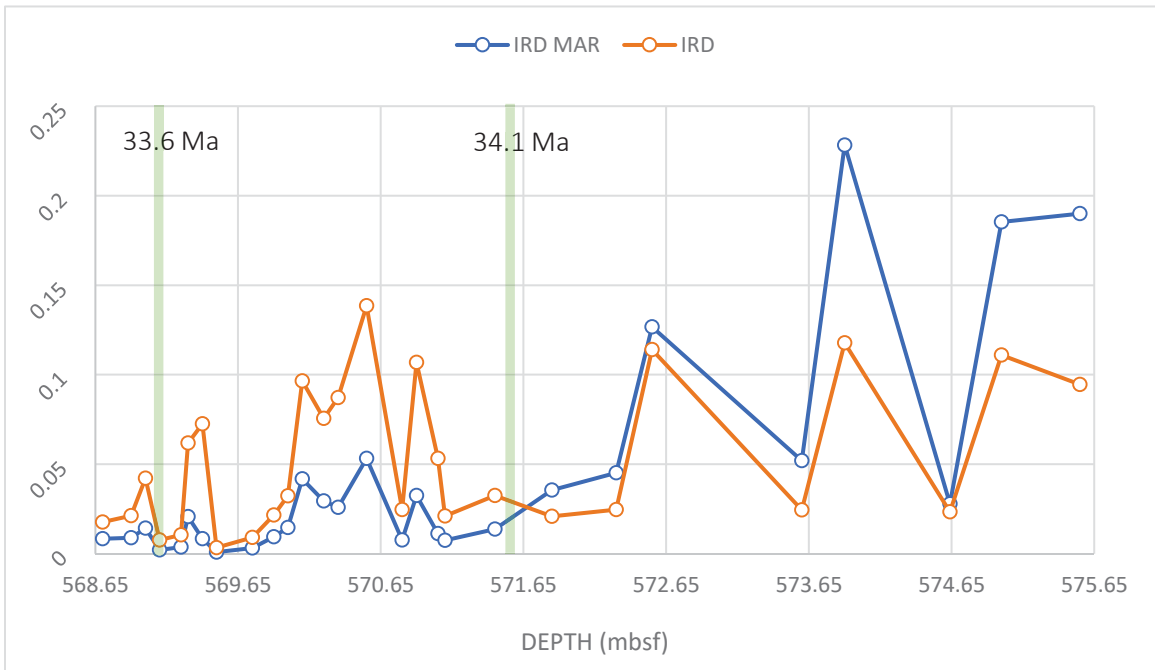
Figure 12: IRD MAR plotted with corresponding IRD fraction against depth. Disparity between plots primarily reflects the decrease in LSR above 571.85 mbsf.
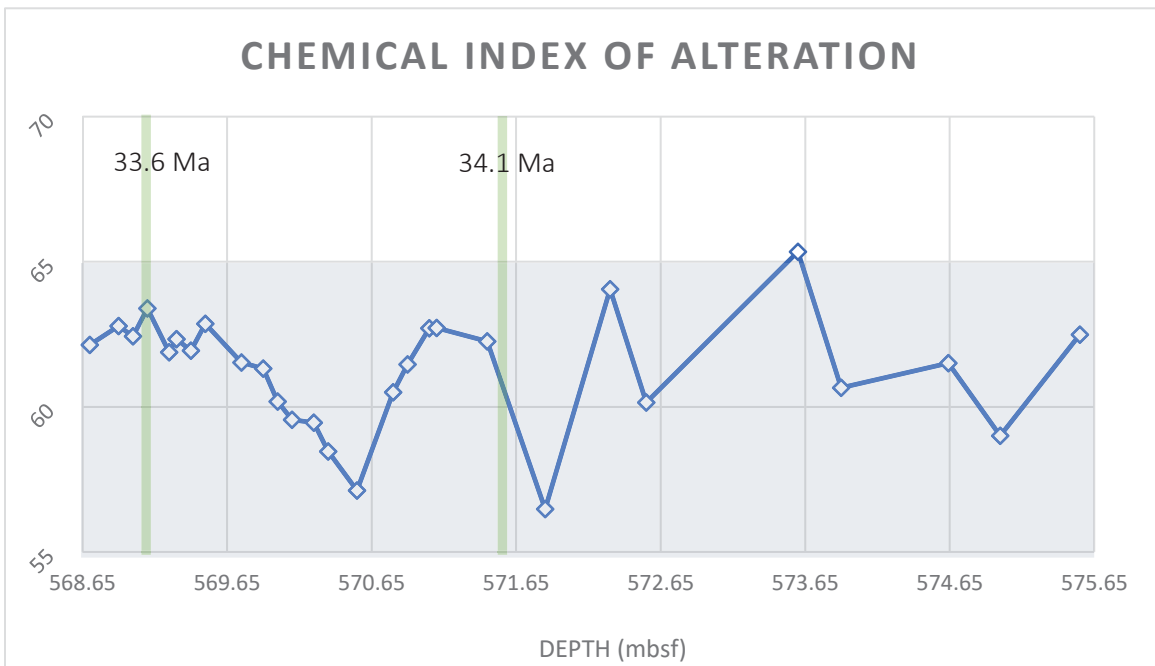
Figure 13: chemical index of alteration (CIA) plotted against core depth; shaded region encompasses values below 65, which denotes a physical weathering regime dominates.

notable drops to 56 and 57 occur at 571.85 and 570.55 mbsf, respectively. All values throughout the core are consistent with a primarily physical weathering regime. To further characterize weathering trends, we can examine trace elements; studies analyzing trace element behavior in critical zone soils show varying degrees of fractionation between elements Rb and Cs in response to surficial weathering processes (McLennan, 2001). Both elements have been observed to behave analogously to K during chemical weathering (e.g., Middelburg et al., 1988; Ma et al., 2011), and McLennan
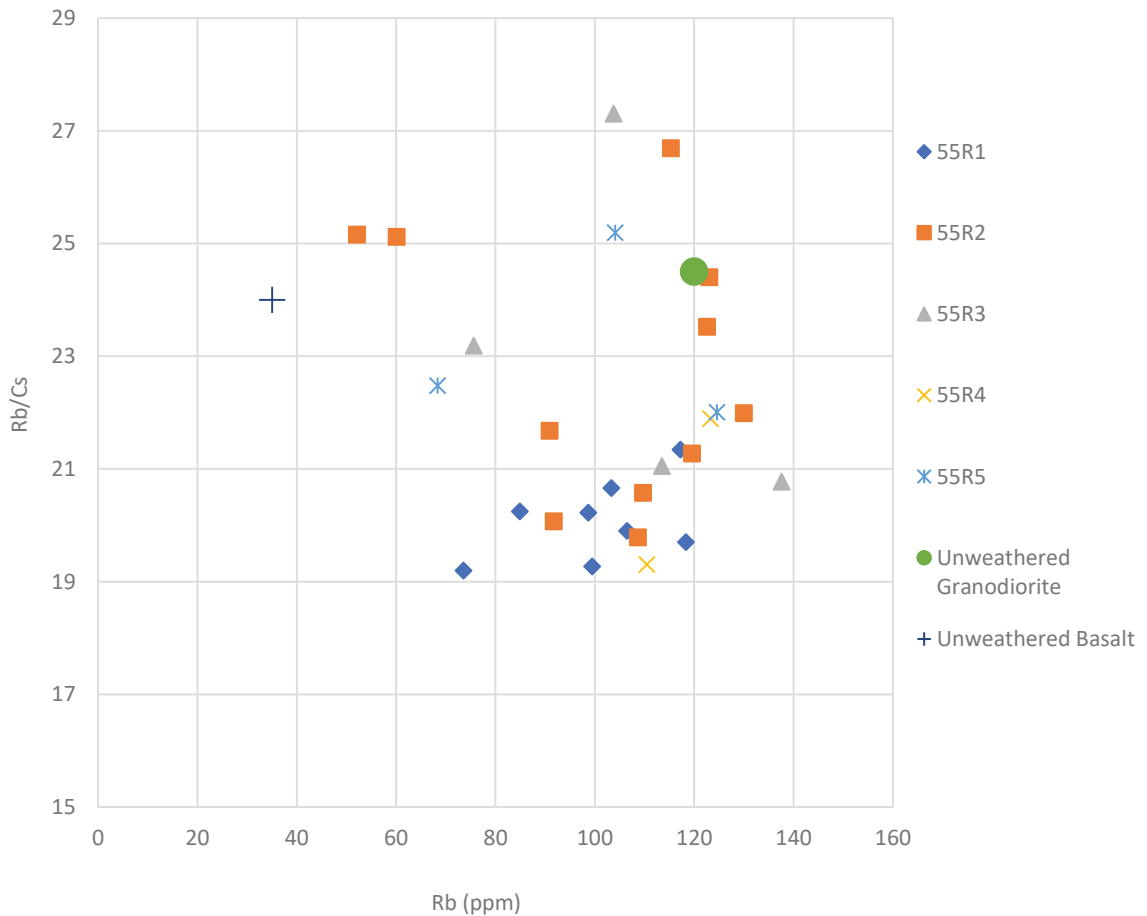
Figure 14: Rb/Cs vs Rb weathering profile of 55R sediments by section after McLennan (2001). Included reference are values for unweathered basalt and unweathered granodiorite.

(2001) asserts upper crust Rb/Cs ratios are decreased in residual sediment as Cs exchanges onto clay minerals when interacting with natural waters. 55R values of Rb/Cs vs. Rb show varying degrees of fractionation with respect to Rb (Figure 14). Samples from section 1 display the least amount of fractionation (Rb/Cs values from 19.2-21.3), while section 2 samples show the greatest variation (19.7-26.7).

3.2.2 *Elemental Enrichments*

The trace and rare earth elements were normalized against data from the upper continental crust (UCC) and average chondrite, respectively. Trace elemental concentrations are considered enriched for values greater than one, and depleted for values below one. Additional plots showing major element data normalized to canonical values for the NASC can be found in the appendix (Gromet et al., 1984).

Overall, enrichment and depletion trends downcore are similar, though Section 1 samples are more uniform and show far fewer elemental enrichments than Sections 2-5 (Figure 15). Slight enrichments in Rb and Cs occur throughout, and to a lesser extent in Sc and V. While some samples show Zr and Hf enrichment in 55R2-R5, both are depleted in R1. Those samples that do not show enriched concentrations of Rb, Cs, Zr, and Hf over UCC values do exhibit lesser amounts of depletion compared to other elements. Pb shows varying degrees of depletion downcore. Elements Co and Ni are depleted in all samples, and Cr in all but one.
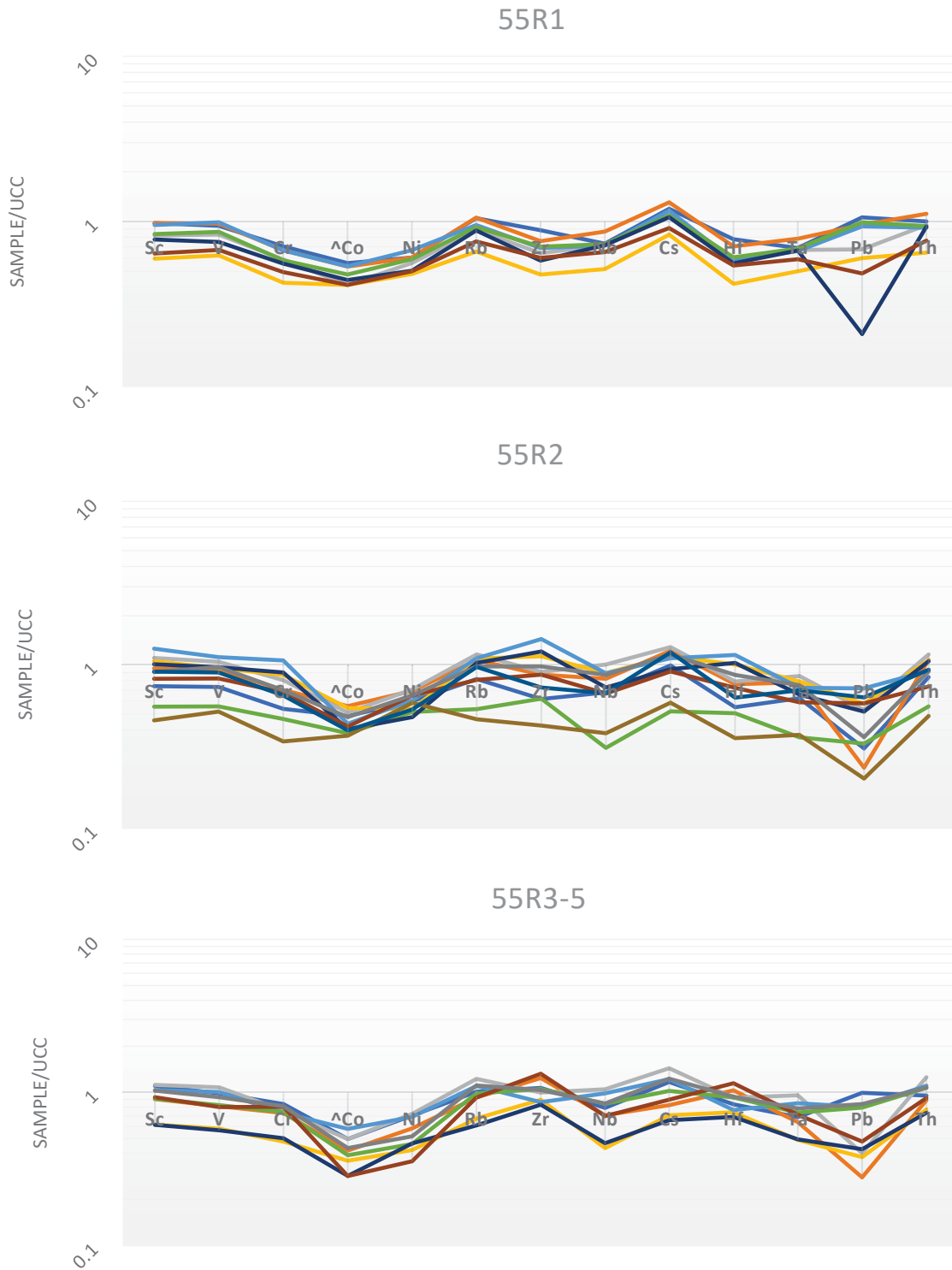
Figure 15. Trace element concentrations of 55R by section, normalized to canonical values of upper continental crust (McLennan, 2001). ^Co denotes only one measurement used in calculations. All other values are based on averages of four instrument runs.
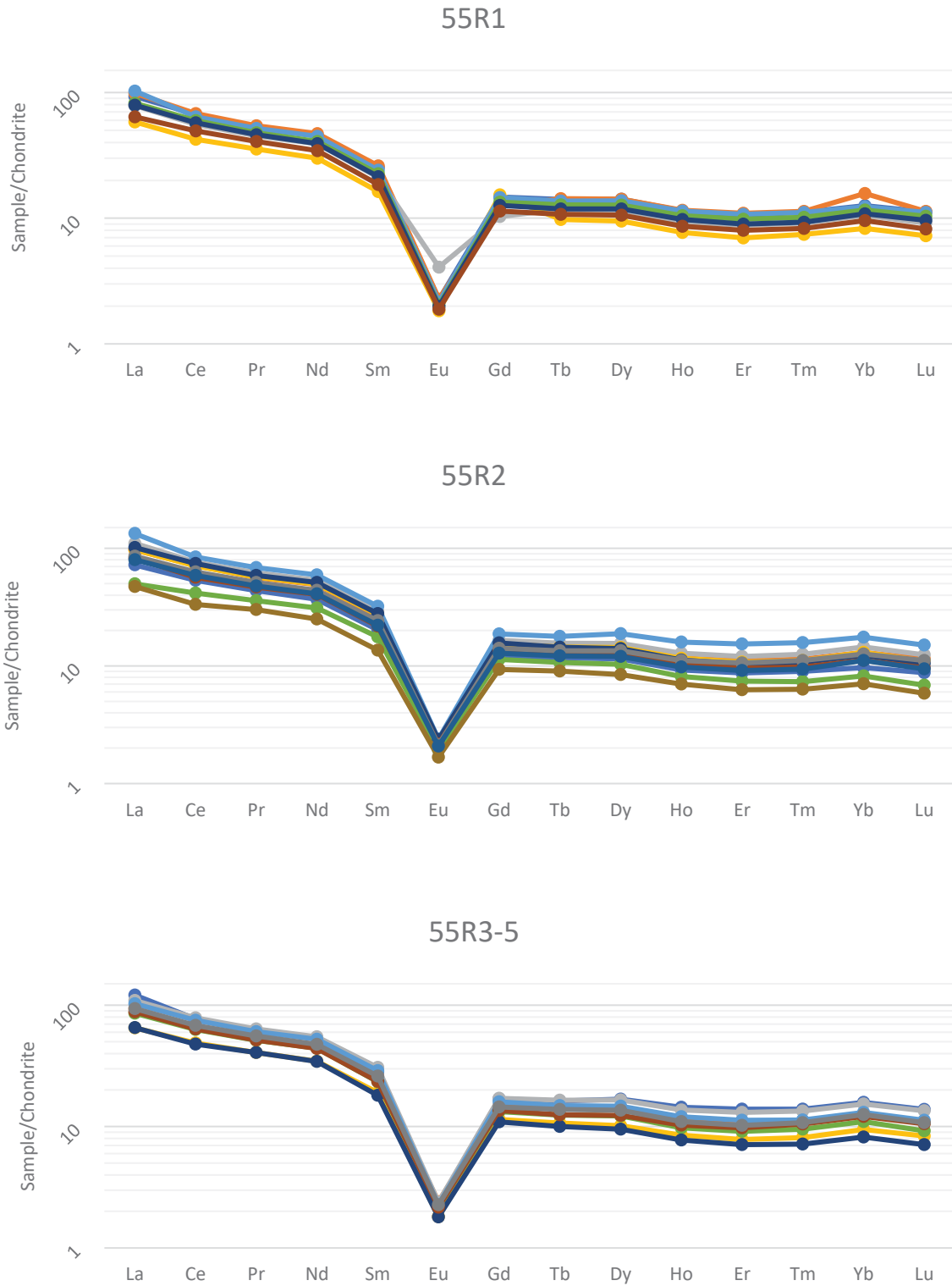
Figure 16: Chondrite-normalized REE concentrations for Core 55R separated by section. Values from Nakamura (1974).

The chondrite-normalized REE plot almost identically downcore (Figure 16).

Most notable is the prominent negative Eu anomaly exhibited by all samples. This

anomaly, denoted Eu/Eu*, is calculated as

$$\frac{Eu}{Eu*} = \frac{Eu_N}{(Sm_N + Gd_N)^{1/2}} \qquad (6)$$

where subscript N denotes normalized values (McLennan, 2001). Enrichment of the light

REEs (La – Sm; LREE) increases slightly downcore while very minor enrichments of

heavy HREEs (Gd – Lu; HREE) remain consistent. The exception here is Yb,

demonstrating a greater degree of enrichment over other HREEs in all samples, which

show consistently flat (i.e., $Gd_N/Yb_N = 1.0$ to 2.0) patterns (McLennan et al., 1993).

3.2.3 *Provenance Constraints*

To determine whether sediment deposited at Site 696 in this core interval came

from one or multiple sources, it is useful to examine immobile, or conservative, elemental

ratios. These elements are least fractionated by weathering processes and diagenesis and

thus retain the geochemical signature of their parent rock (Piper & Bau, 2013;

McLennan, 2001). Major elemental ratio Ti/Al has been used to confirm similar

provenance in paleosols, despite variations in weathering on parent material (Sheldon and

Tabor, 2009). Figure 17 shows Al_2O_3 plotted against TiO_2, supplemented by immobile

Sc. Both elements show a linear decrease in concentration with respect to Ti; the absence

of obvious groupings suggests 55R sediments are of a common origin (Figure 17).
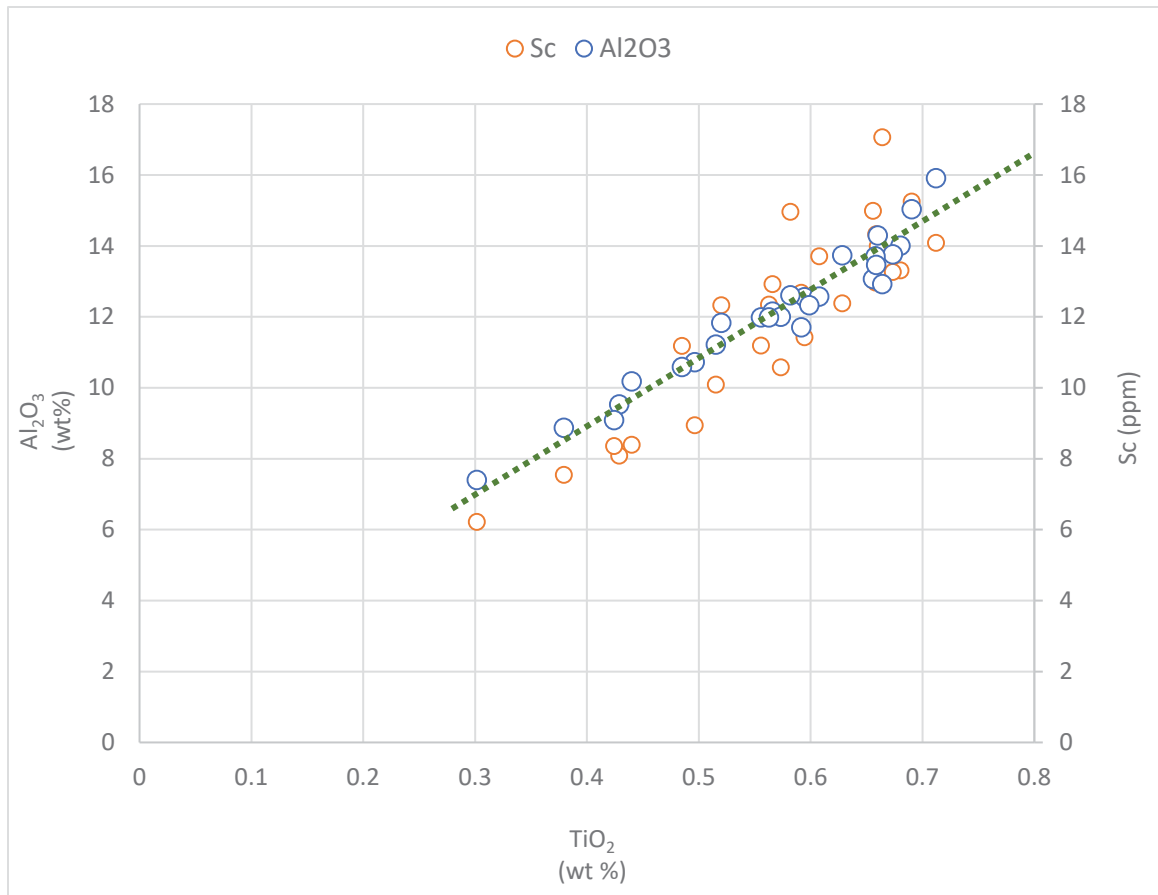
Figure 17. Immobile major and trace ratios plotted together to evaluate variation in sediment provenance. Both Al$_2$O$_3$ and Sc plot well along the line of best fit, indicating a consistent elemental ratio in 55R samples.

The elemental enrichment data presented in 3.2.3 indicate sediment of felsic origin. High La$_N$/Yb$_N$ ratios (avg. 7.35), greater enrichment in LREEs over HREEs, prominent negative Eu/Eu* values throughout (avg. 2.2), and low-magnitude deviations of trace element concentration from UCC values all support the terrigenous fraction in 55R is felsic in nature (Potter et al., 2005; McLennan et al., 1993). To further examine degree of felsic versus mafic composition, samples were plotted on a Th/Sc versus Zr/Cr diagram. Th and Zr are enriched in such felsic minerals as feldspars, while Sc and Cr are

prevalent in mafic minerals including olivines and amphiboles (Potter et al., 2005).

Additionally, the low solubility of these elements makes them useful indicators in

sediment provenance studies (Potter et al., 2005). For comparison, averages from
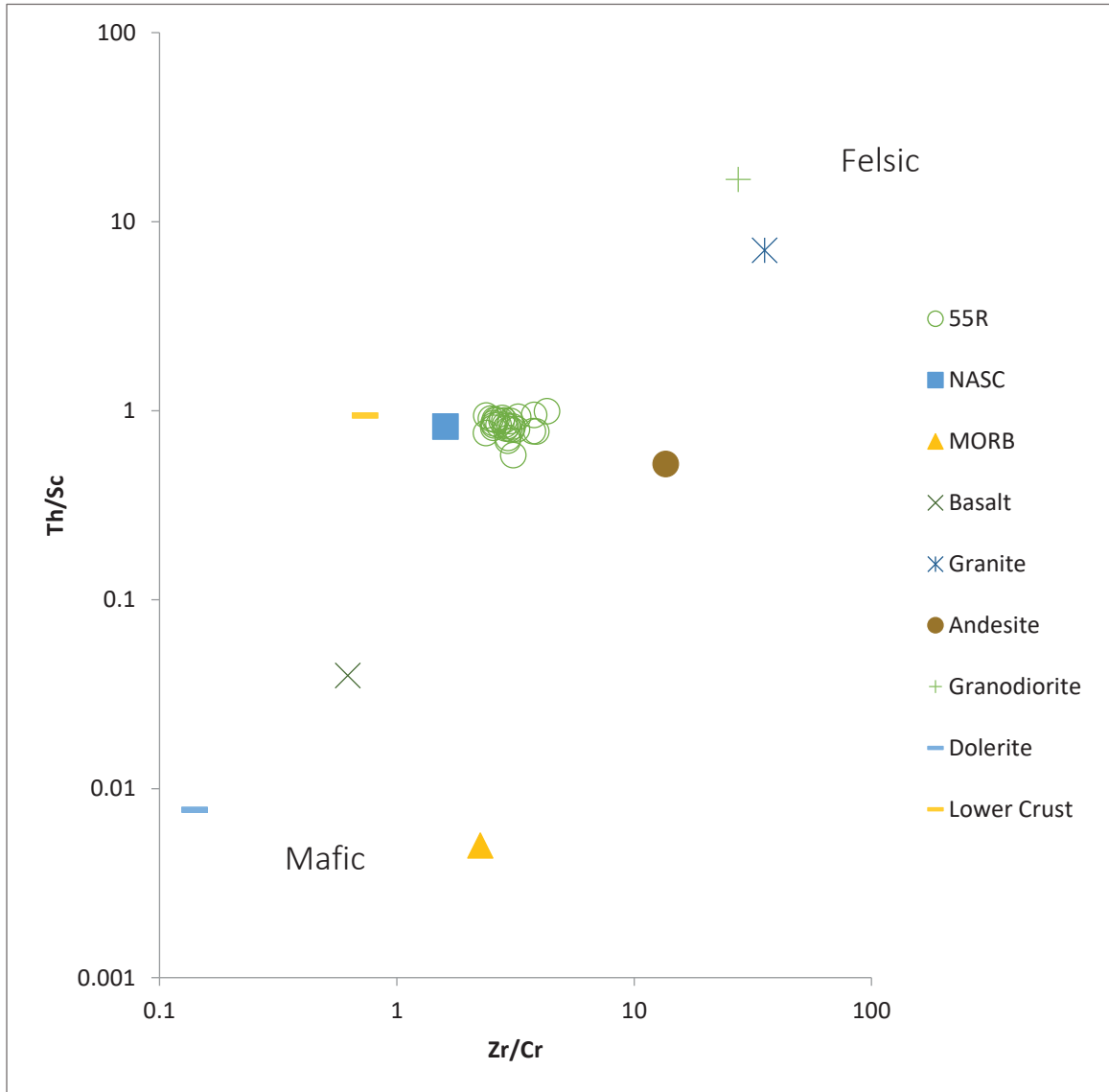
Figure 18: Th/Sc versus Zr/Cr plot featuring 55R samples in relation to USGS standards and additional composites. Composite data from Gromet et al., 1984; Pearce, 1983; Wedepohl, K.H., 1985. After McLennan et al., 1993.

various lithologic composites and USGS standards were plotted as well (Figure 18). 55R samples plot well with each other, confirming a similar composition. This projection does not support mafic parent rocks like dolerite and basalt, and shows 55R contains less felsic material than standard granite and granodiorite. samples most closely align with values of the NASC, and to a lesser extent, lower crust.

To further characterize sediment nature, 55R ratios of Th/U vs. Th are compared against values of turbidite muds from various tectonic settings (McLennan et al., 1993). 55R values agree with published values of active margin turbidite muds, the bulk of which showed Th values between 5 and 10 (Figure 19; McLennan et al., 1993).
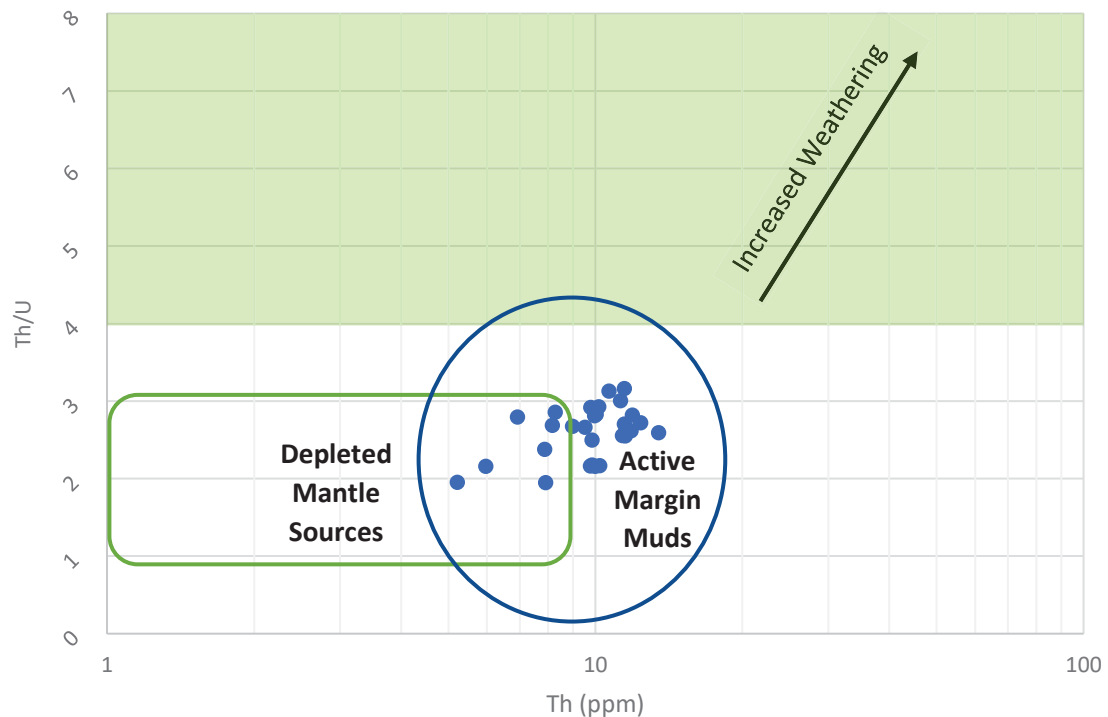
Figure 19: Various tectonic settings and associated Th/U vs. Th values. Th/U ratios above 4 represent Upper Crust composition, increased weathering conditions are reflected in elevated Th/U ratios, and low Th/U signify depleted mantle sources (McLennan, 1993).

Finally, provenance constraints were applied by comparing 55R data with published ratios from East and West Antarctic formations in the Weddell Sea sector. Two plots were constructed based on trace and REE data available. Figure 20 shows Th/Ni plotted against Zr/Cr. There is strong agreement between 55R samples and both the Hope Bay and Cape Legoupil formations of the northern Antarctic Peninsula, which consist of nearly unaltered mudstones and sandstones (Castillo et al., 2014). Samples from 55R do not plot well with either the granodiorite or the granite from the Ellsworth-Whitmore Mountains of West Antarctica (Vennum and Storey, 1987), suggesting 55R is more intermediate in composition than surrounding granitic suites.

A plot of La/Th against Hf reveals 55R sediments do not geochemically resemble the metadiorites or metagranites from the Shackleton Range of East Antarctica (Figure 21, after Floyd and Leveridge, 1987). 55R samples do, however, plot reasonably well with granitic gneisses from the North Terrane region of the Shackleton Range and homogenous granodioritic migmatites from Dronning Maud Land. Again, sample ratios agree most notably with more local sources from the Antarctic Peninsula; the Latady and Mount Poster Formations of the Southern peninsula are characterized as upper-crustal granitoids and granodiorites (Vennum and Rowley, 1986). These agreements support a felsic origin for 55R samples. Samples show a range of Hf values between 2 and 7 ppm, and La/Th ratios are quite consistent, except for four samples with elevated La concentrations (Figure 21).
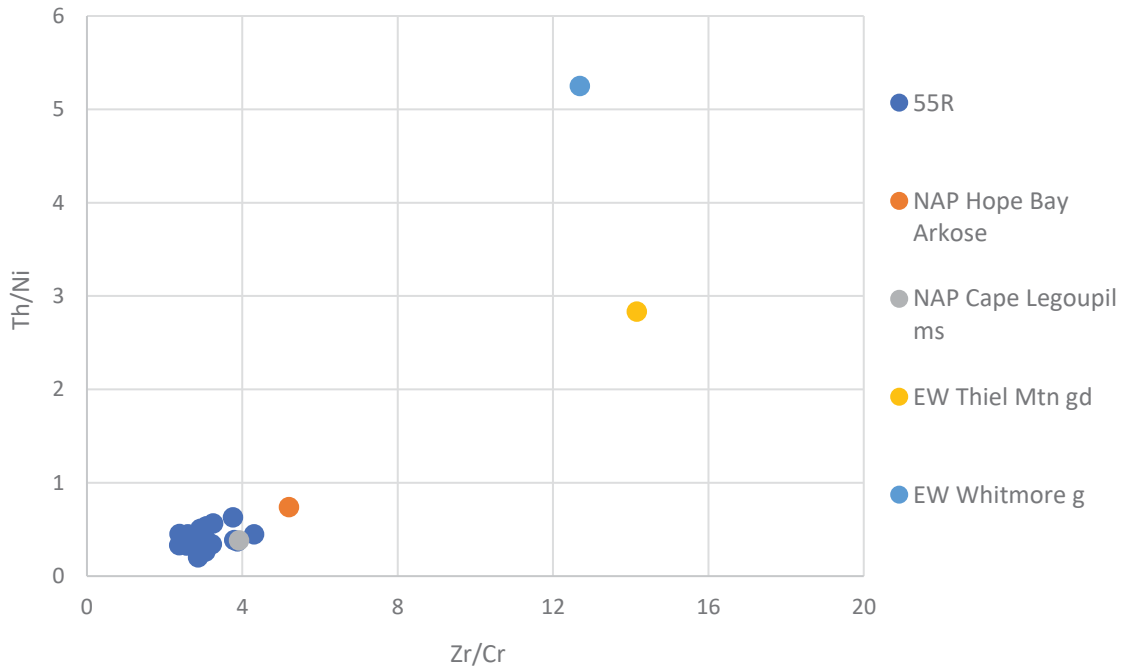
Figure 20. Th/Ni vs Zr/Cr plot showing 55R samples in relation to northern Antarctic Peninsula (NAP; Castillo et al., 2014) and Ellsworth-Whitmore formations (EW; Vennum and Storey, 1987). Gd = granodiorite, g = granite, ms = mudstone.
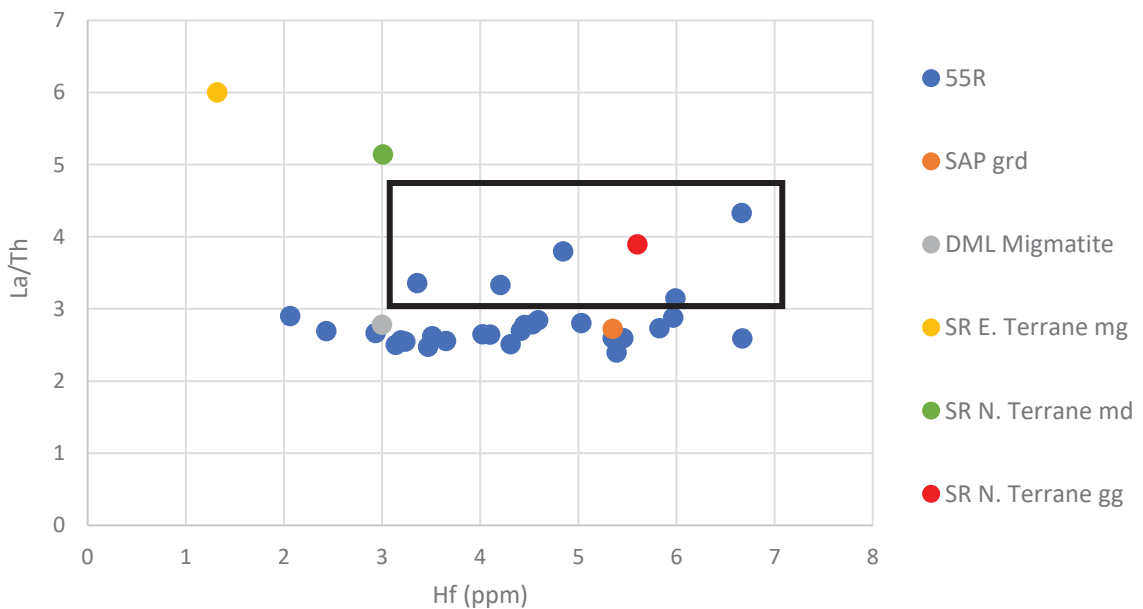
Figure 21. La/Th vs Hf plot showing 55R samples in relation to southern Antarctic Peninsula (SAP), Dronning Maud Land (DML), and Shackleton Range (SR) formations. Grd = granodiorite, mg = metagranite, md = metadiorite, gg = granitic gneiss (Will et al., 2010; Paulsson and Austrheim, 2003; Vennum and Rowley, 1986). 55R samples with elevated La/Th ratios are boxed.

41

4. DISCUSSION

4.1 Paleoclimate Conditions

4.1.1 Depositional Environment

Results from the laser particle size analysis can be interpreted to infer plausible environmental settings during time of sediment deposition. The pie charts shown in Figure 11 demonstrate relatively consistent grain size distributions throughout all sections of 55R. This suggests that from 34.3 Ma to 33.52 Ma, the shelf of the SOM was not subject to major changes in relative sea level (RSL). Low clay percent, a reasonable sand fraction, and the presence of glauconite downhole (57R) indicate a shallow water environment; indeed, reconstructions suggest paleodepth of ~550 m (Wei and Wise, 1990). However, when 55R samples are plotted on a ternary diagram with downhole samples dated up to 36.63 Ma, a new trend emerges (Figure 22). This shift in distribution can be characterized as a fining upward sequence, transitioning from predominantly sand- and silt-size grains to majority silt-sized grains with roughly equal, lesser percent contributions from silt- and clay-sized grains.

Fining upward sedimentary sequences generally indicate a transgressive environment, where the increase in water depth allows for the settling of finer particles (Boggs, Jr., 2011). However, research demonstrating eustatic sea level fall (Houben et al., 2012; Katz et al., 2008) combined with evidence for significant ice development during the EOT do not support this interpretation. Relative SLR on the SOM shelf may therefore be explained by crustal subsidence in response to regional glacial expansion;
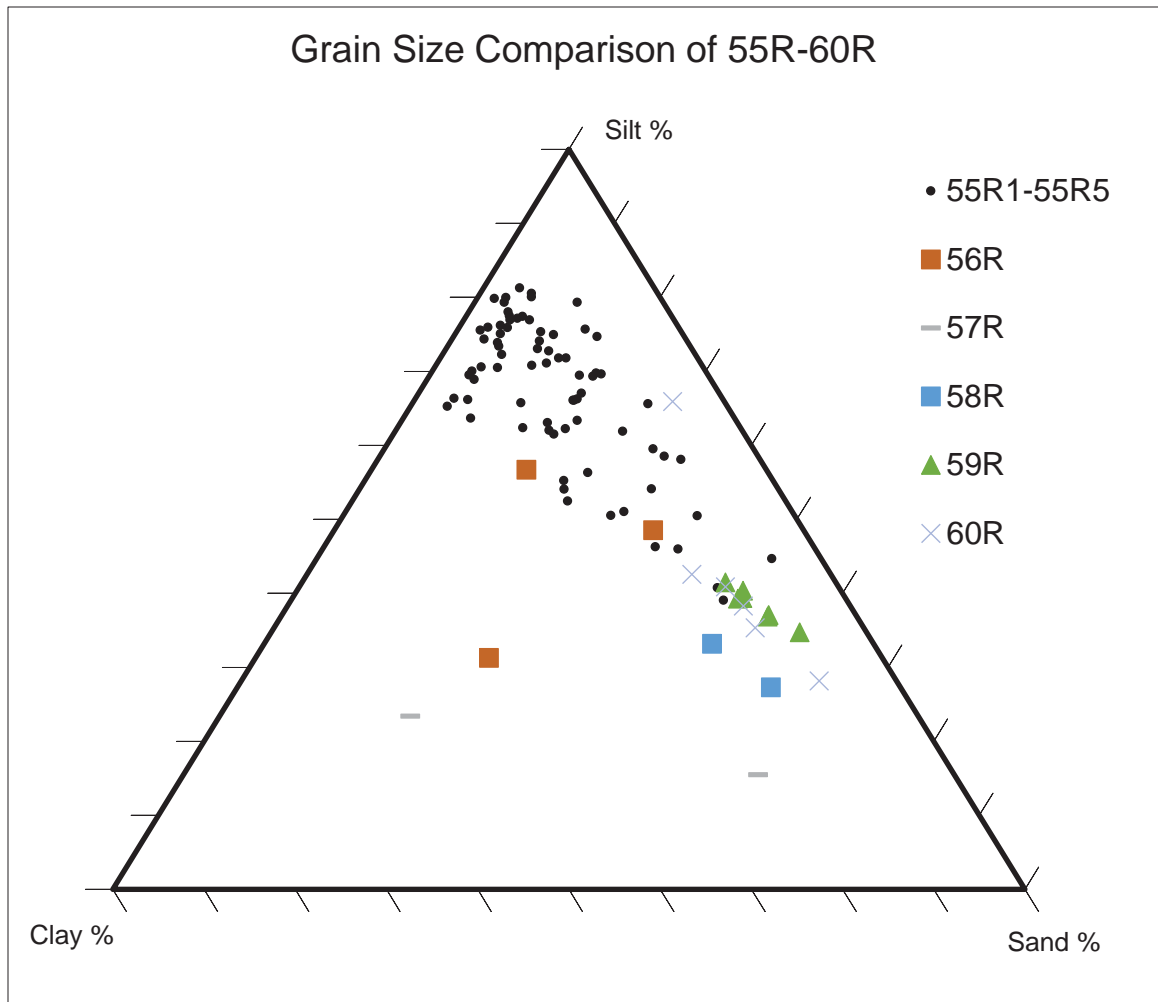
Figure 22: Ternary diagram comparing particle size distribution of samples from 55R to downhole samples (Light, 2017; unpublished data from D. Cone). While 55R samples exhibit dominant (~70%) silt fraction, distribution downhole skews towards sand contribution in excess of 50%.

Stocchi et al. (2013) modelled changes to relative sea level (RSL) in Antarctic shelf environments in response to ice-sheet growth, which demonstrated initial shoaling followed by subsidence. Their simulations were in agreement with observed East Antarctic shelf sediments, and while neither their models nor their sedimentological

analysis investigated EOT conditions in the Weddell Sea sector, similar processes may have occurred proximal to Site 696 (Stocchi et al., 2013).

Because of the timescale represented by this sedimentary sequence, change in RSL may better be explained by regional tectonic expansion. Initial rifting of the SOM from the Antarctic Peninsula is thought to have begun in the late Eocene (Eagles and Livermore, 2002; King and Barker, 1988). Particle size data shows a permanent decline in significant (42-63%) sand contribution following ~34.9 Ma, which is temporally consistent with initial stages of SOM rifting beginning at ~37 Ma (King and Barker, 1988). Crustal subsidence associated with regional tectonism is therefore another plausible driving factor behind increasing water depth on the SOM margin from the late Eocene to early Oligocene (Livermore et al., 2005).

4.1.2 *Weathering Regime*

Following the Paleogene-Eocene Thermal Maximum (PETM) at 55.8 Ma (Vandenburghe et al., 2012), chemical weathering was prevalent across the Antarctic continent, as evidenced by high mean atmospheric temperatures (MAT) and precipitation from paleoclimate reconstructions (e.g., Light, 2017, Passchier et al., 2017, Feakins et al., 2014) and kaolinitic clay assemblages from East and West Antarctic margins (Houben et al., 2013; Shipboard Scientific Party, 1988). One of the strongest pieces of evidence for the climate transition at 34 Ma is observed shifts in clay mineralogy, in Antarctica and elsewhere (Houben et al., 2013; Wang et al., 2013). Where kaolinite and smectite are indicative of chemical weathering and extensive breakdown of feldspar minerals, illite and chlorite signify a physical weathering regime (Robert and Maillot, 1990).

The Site Report for 696 indicates clay mineralogy in 55R is dominated by smectite (~70%), with ~10% chlorite and 20% illite (Robert and Maillot, 1990). There is a noticeable increase in illite and to a lesser extent, chlorite minerals in 55R as compared to 696 cores of the mid- to late-Eocene (Robert and Maillot, 1990). The preservation of these minerals in conjunction with consistently glacial CIA values reflect a more arid, cooler climate where terrigenous weathering is less governed by chemical processes. The coincidence of 55R's lowest CIA value with the initial drop in LSR at ~34.1 Ma provides further evidence for increasing terrestrial climate deterioration.

This steady glacial weathering signature throughout 55R agrees with other climate reconstruction studies for the Antarctic Peninsula, which indicate decreasing temperatures and precipitation rates prior to the EOT (e.g., Feakins et al., 2014, Anderson et al., 2011). Weathering conditions in the northwestern Weddell Sea sector are also consistent with those reconstructed for the Prydz Bay region, where shelf sediments begin to reflect glacial CIA values as early as ~34.2 Ma (Passchier et al., 2017). Earliest Oligocene sediments from the Wilkes Land Margin of East Antarctica also exhibit CIA values within the glacial range (Light, 2017), confirming large-scale regional cooling across the EOT.

In the Ross Sea sector, however, an observed shift in clay mineralogy denotes the transition to a dryer, cooler environment did not occur in West Antarctic until 32.8 Ma (Galeotti et al., 2016). It has been suggested West Antarctica maintained a warmer climate longer than did East Antarctica because it was affected by southward flowing surface currents (Robert and Maillot, 1990). CIAs calculated from 55R suggest regional cooling and the shift from chemical to physical weathering in the Weddell Sea sector

occurred earlier than 34.3 Ma. This also indicates climatic conditions favoring glacial

expansion dominated in this region earlier than other studies show, therefore offering

support for asynchronous climate deterioration and associated ice sheet development

across the Antarctic continent.

4.1.3 *Particle Size Distributions*

The combination of significant (~70%) silt contribution to 55R samples with

corresponding CIA values consistently within the glacial range indicates sediment

delivered to the SOM margin maintains a glaciogenic signature. Under a warm, wet,

climate where chemical weathering prevails, silt-sized minerals are likely to break down

to clay minerals (Thiry, 2000). The preservation of the silt fraction in 55R samples

indicates environmental conditions were not conducive for pedogenic completion, as is

confirmed by CIA values below 65. Passchier et al. (2017) assert detrital material

associated with glacial erosion (i.e., glacial rock flour) is found predominately in the silt

fraction. Low clay percents throughout the core suggest a relatively shallow depositional

environment and strong physical weathering conditions.

Eccentricity and obliquity geometries yielded cooler summers and provided

environmental conditions conducive for high latitude ice growth during the EOT (Coxall

et al., 2005), and orbitally-paced glacial advance and retreat cycles during this transition

have been recognized in East and West Antarctic margin sediments (e.g., Passchier et al.,

2017, Galeotti et al., 2016). 55R exhibits regular fluctuations in sand percent, with

spacings every ~60 kyr prior to 34.1 Ma, and every ~170 kyr after (Figure 23). This

implies 55R captured local, land terminating glacial responses to changes in orbital

configurations; peaks in sand percent are interpreted as representing periods of regional
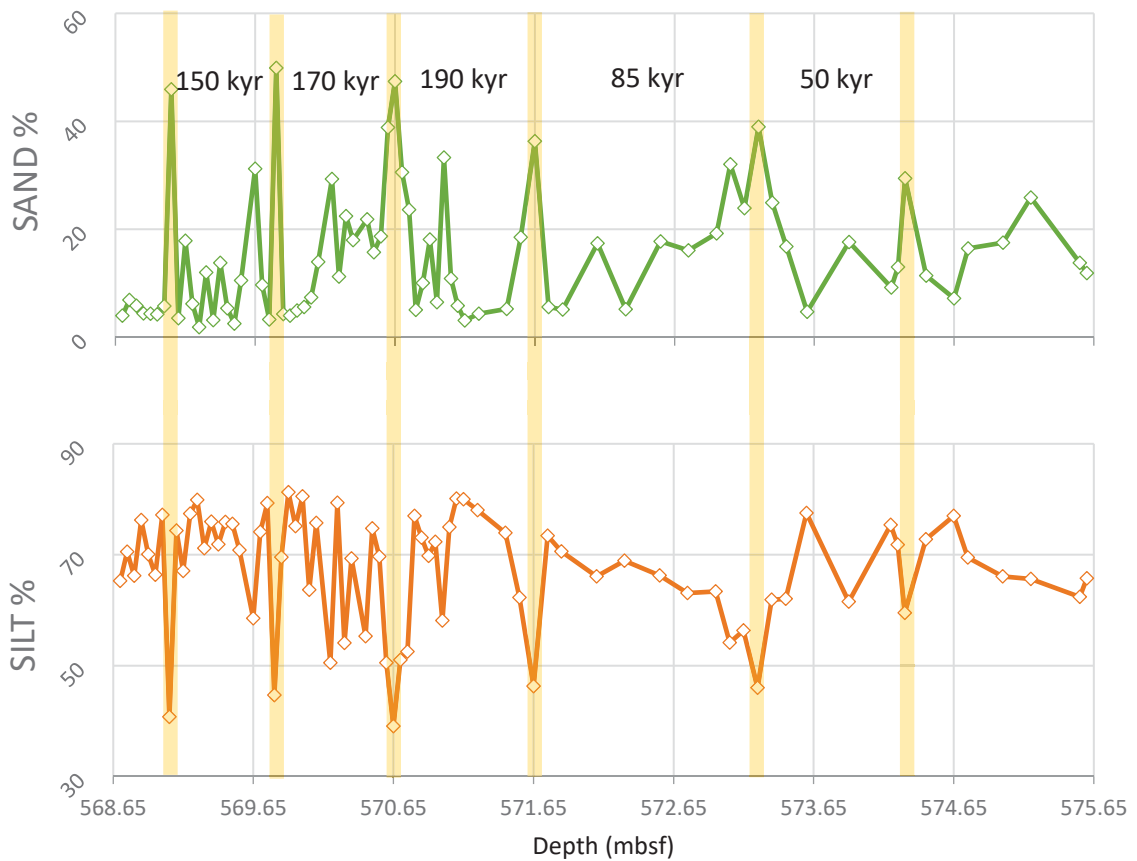
Figure 23: Regular increases in sand percent and corresponding decreases in silt percent throughout 55R. Time between sand peaks are labeled, and suggest correlation to eccentricity cycles.

glacial advance, where enhanced erosion supplied coarser detrital material to the SOM margin. Additionally, contribution from the sand fraction increases upcore, indicating stronger and more stabilized glacial conditions with each orbital cycle. A 2006 study analyzed stable isotope ratios from an equatorial Pacific drill core, and identified eccentricity cycles throughout the Oligocene as occurring in 96 kyr, 127 kyr, and 405 kyr intervals (Pälike et al., 2006). Comparable time between 55R sand peaks suggests regional glacial advance was correlated with the eccentricity band.

4.2 **Sediment Source**

4.2.1 *Provenance*

Results of the geochemical analysis for Core 55R indicate that sediment likely has a common origin. Similarities in both TiO_2/Al_2O_3 and Th/Ni versus Zr/Cr ratios demonstrate a consistency in bulk immobile element geochemistry. Additionally, paleomagnetic reconstructions of the location of the SOM during the EOT strongly suggest the majority of terrigenous sediment originated from local Antarctic Peninsula formations. While it is common for mudstones to include constituents of varied sources due to particle mixing that occurs with long-distance transport of fine grains (Potter et al., 2005), the geochemical similarities in the mud fraction of 55R suggest little variability during grain erosion and transport processes.

REE normalized patterns demonstrate several features characteristic of felsic material (i.e., high LREE/HREE, negative Eu* anomaly, flat HREE). However, provenance plots of felsic versus mafic ratios (Figures 20, 21) suggest 55R sediments are slightly more intermediate than felsic Weddell Sea sector formations. Mudstones of the Trinity Peninsula Group also show felsic REE-chondrite normalizations; a thorough geochemical investigation into several formations of the northern Antarctic Peninsula revealed these metasedimentary rocks are also of felsic volcanic origin, and range from tonalitic to granodioritic compositions (Castillo et al., 2014). The likeness of Th/U versus Th values between 55R samples and active margin muds (Figure 19, after McLennan et al., 1993) strongly support local provenance, as the SOM and northern Antarctic Peninsula were experiencing significant rifting during the EOT. While both the Antarctic Peninsula and EWM microplates rotated and translated synchronously during the breakup

48

of Gondwana, the latter reached its present-day position by the late Cenozoic (Fitzgerald, 2002). As East Antarctic formations in the Weddell Sea sector were tectonically stable during the EOT, it is less likely 55R sediments are associated with these distal locations. Elevations reconstructed in the Northern Antarctic Peninsula for the EOT (Wilson et al., 2012) indicate topographic relief comparable to DML and the TAM, which models suggest were nucleation points for late Eocene glaciation (DeConto and Pollard, 2003). Interpretations for sustained glacial presence in the Antarctic Peninsula region at this time are therefore reasonable.

4.2.2 *IRD MAR*

Provenance studies from the Antarctic margin have confirmed IRD MAR generally reflects local glacial advances (e.g., Williams et al., 2010; Cowan et al., 2008). 55R shows high peaks at the base of the core, and a decrease in IRD MAR following 34.1 Ma. This implies the presence of tidewater glaciers in the northern Antarctic Peninsula c. 34.3 Ma. Drill core and seismic interpretations from SHALDRIL cruises I and II also provide evidence for tidewater glaciers in the northern Antarctic Peninsula prior to the EOT (Anderson et al., 2011). Furthermore, marine sediments and diamicton deposits from Seymour Island in the northern Antarctic Peninsula were given age constraints around the EOT, and provide additional evidence for significant regional ice presence in the late Eocene (Ivany et al., 2006).

To clarify IRD MAR interpretation, it is useful to also examine grain uniformity. Passchier (2011) explains that the coincidence of a high IRD MAR value with a low uniformity reflects elevated sand percent resulting from the removal of fines by currents. 55R uniformity remains low throughout the core, apart from two spikes where uniformity

exceeds 8. While these spikes do align with peaks in sand percent, they occur upcore of the decrease in LSR, and their corresponding IRD MAR values are low. These alignments can be interpreted as enhanced glacial erosion coupled with a temporary decrease or shift in bottom-water currents, rather than glacial advancement onto the shelf and production of local icebergs. Similar distributions from the Wilkes Land margin, featuring comparable sand percent (45-50%), high sortable silt contribution, and low (<4) uniformity values, have been interpreted as the effect of sediment sorting by current interaction (Passchier et al., 2018). Additionally, the sizable effect of LSR on IRD MAR demonstrated in Figure 12 presents a caveat in the dependability of the proxy within this study; identifying additional age tie-points throughout 55R would increase resolution of changes to sedimentation rate, and improve reliability of IRD MAR during this interval.

A recent (2016) study of 696 cores encompassing the late Eocene to early Oligocene utilized fingerprinting techniques, including zircon U-Pb dating and apatite thermochronometry, to investigate provenance of sand grains found above and below 55R. They identify microtextures associated with IRD in downhole cores 62R-59R, trace grains to sources in the EWM and the shelf region of DML, and assert the majority of detritus was supplied to the SOM via ice rafting. Their results indicate substantial ice volume and glacial calving in the southern Weddell Sea embayment as early as 36.5 Ma (Carter et al., 2016). While 55R sediments provide evidence of a cool climate and a physical weathering regime, elemental ratios do not reflect provenance variation that would support widespread marine-terminating glaciation in the late Eocene. Carter et al. (2016) note that downhole of 55R, microtextures they attribute to IRD processes may also result from silica diagenesis or glaciomarine current reworking. It may therefore be

useful to incorporate additional analytical techniques to cores investigated by Carter et al. (2016) with the resolution applied in this study.

4.2.3 *Elemental Enrichments*

Elemental enrichments and depletions in 55R sediments are most likely attributed to compositional nature and weathering-related processes. Depletions in mafic elements Ni, Cr, and Co throughout are consistent with sediment that derived from a felsic to intermediate source (McLennan, 2001). Varying degrees of minor enrichment and depletion of Rb and Cs, as well as the Rb/Cs fractionation displayed in Figure 14, are explained by grain-size partitioning of these elements (McLennan, 2001). The bulk of 55R samples show decreased Rb/Cs values compared to unweathered material, which is consistent with silt-rich sediment; elevated Rb/Cs ratios above 25, however, are found in those samples with a greater sand fraction and indicate less mature material (Figure 24). Similarly, samples plotting with slightly elevated La/Th ratios in Figure 21 are driven by increased La concentrations. La is a REE, which are typically more enriched in the fine fraction than in coarse material (Potter et al., 2005). Figure 25 shows the distribution for these samples are dominated by very fine silts with notable clay contributions.

The linear trend represented in Al/Ti and Sc/Ti ratios indicates a consistent ratio between these elements, demonstrating immobile behavior and supporting a common parent material (Sheldon and Tabor, 2009). The similarities between REE normalized plots and those typical of felsic rock types confirm the lithogenic origin of 55R sediments (Piper and Bau, 2013), as does the absence of Mn enrichments (see appendix), which are common in pelagic sediments as a result of biogenic processes.
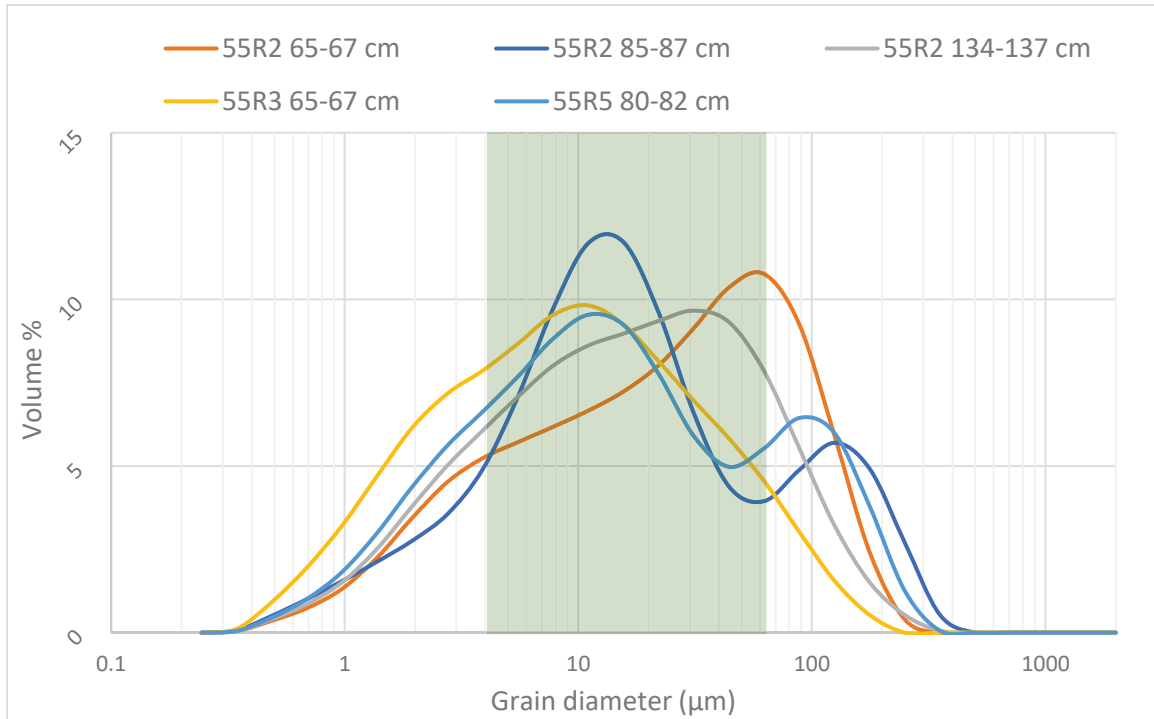
Figure 24: Grain size distributions for samples exhibiting elevated Rb/Cs ratios. Silt fraction is shaded; note samples with bimodal distributions, and significant volume contribution from the sand fraction.
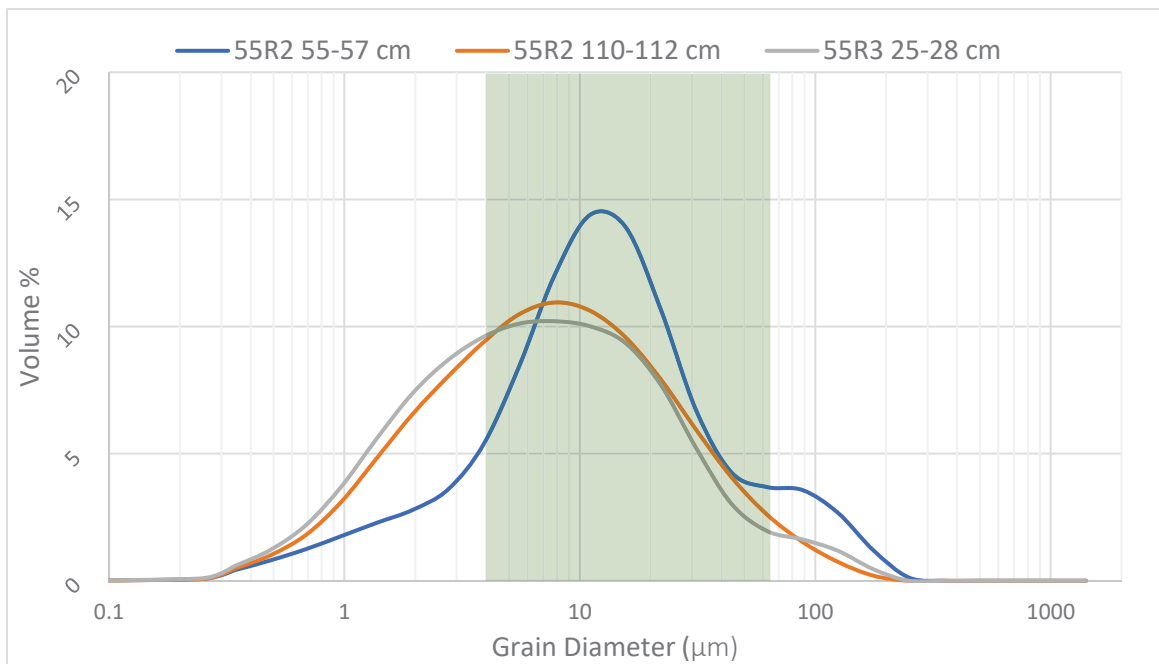
Figure 25: Grain size distributions for samples showing elevated La/Th ratios. Silt fraction is shaded; samples are dominated by very fine silt and significant clay contributions, accounting for enriched concentration of La.

Zr and Hf both show slight enrichments throughout 55R. These elements are typically associated with heavy mineral assemblages like zircon and rutile, and are more commonly enriched in the coarse fraction (silt, fine sands) than in the clay fraction (McLennan, 2001; McLennan et al., 1993). Enrichments are therefore consistent with 55R samples which are dominated by silt. Zr enrichments may also be explained by addition of zircon via sediment recycling (McLennan et al., 1993); Zr/Sc versus Th/Sc ratios of 55R samples and discrimination fields from McLennan et al. (1993), however, indicate Zr enrichment is more likely attributed to grain size partitioning than sediment recycling (Figure 26). This serves to strengthen the validity of the biostratigraphic age
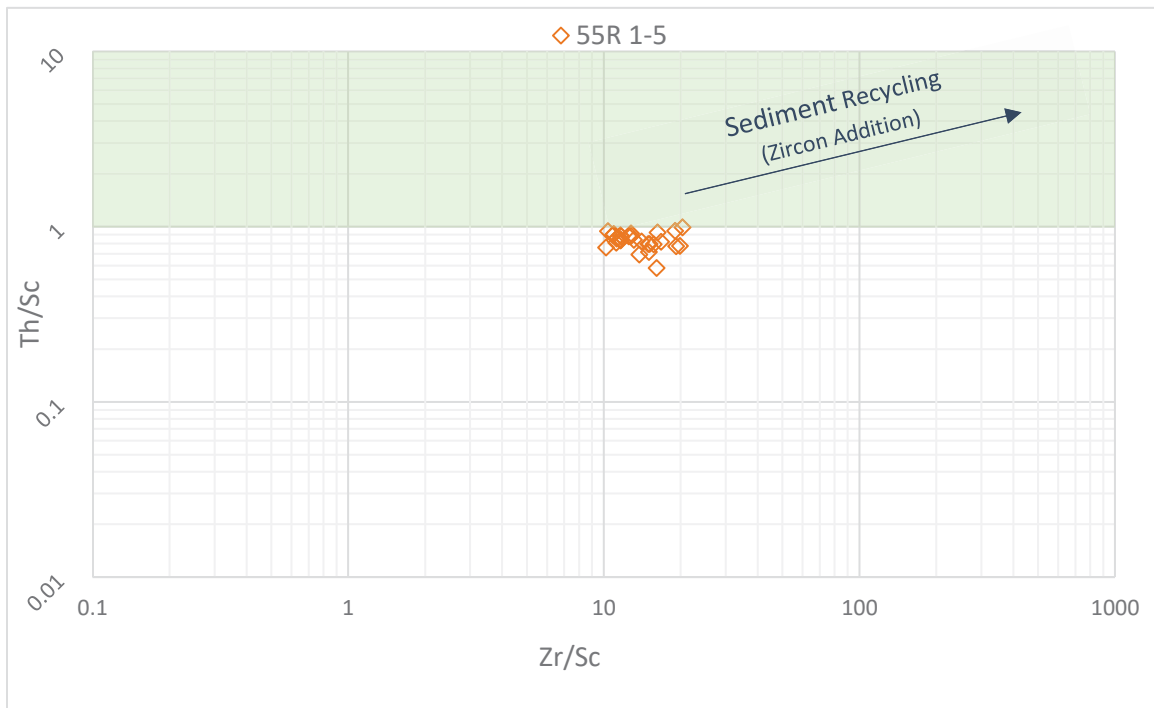
Figure 26: Th/Sc versus Zr/Sc plot demonstrating Zr enrichments in 55R samples are not likely attributed to zircon addition through sediment recycling (McLennan et al., 1993). Shaded region represents values of the UCC.

model applied to Site 696 (Houben et al., 2013), as recycling of late Eocene dinocyst assemblages found downhole is also unlikely. Furthermore, active margin samples are less susceptible to recycling and these results are therefore consistent with Th/U versus Th plots (McLennan et al., 1993).

5. CONCLUSIONS

The multi-method analysis of well-dated shelf sediments from the SOM spanning the EOT presented here improves the understanding of glacial dynamics in the Weddell Sea sector across this climate transition. From 34.3 to 33.52 Ma, the northern Antarctic Peninsula and SOM were experiencing a cool, arid climate dominated by a physical weathering regime. Sedimentation in this region was heavily influenced by wet-based mountain glaciation, as evidenced by substantial contribution of glacial rock flour and CIA values below 65 throughout the core. Peaks of significant sand contribution indicate glaciers were orbitally influenced and cyclically advanced into valleys and perhaps even terminated at the coast. While these results agree with evidence for alpine and potentially tidewater glaciers in the Peninsula during the late Eocene (Anderson et al., 2011), the low sedimentation rates following 34.1 Ma at Site 696 are not consistent with those associated with full-scale glacial conditions in the Weddell Sea sector (Huang et al., 2014).

Recent investigations into Site 696 sediment provenance through the Late Eocene-Early Oligocene identify East and West Antarctic sources and grain transport as IRD (Carter et al., 2016), but geochemical and sedimentological analysis within 55R suggests a local origin. Felsic/mafic ratios most resemble mudstones of the northern Antarctic Peninsula, and Th/U vs. Th values plot analogously to those associated with active margin muds. Sediment exhibits low uniformity throughout, suggesting that while

regional glacial advance provided the initial mechanism for erosion, transport and sorting were controlled by other processes; possibilities include turbidity currents and sorting by bottom current winnowing. Similar sorting and weathering processes are also attributed to elemental enrichments and depletions, rather than changes in sediment provenance.

Core 55R sediments show evidence for significant glacial presence in the northwest region of the Weddell Sea throughout the EOT, consistent with results of similar studies in the Prydz Bay, Wilkes Land Margin, and Sabrina Coast regions (Passchier et al., 2017; Light, 2017; Gulick et al., 2017). These results therefore support large-scale regional cooling and glacial expansion prior to the ~34 Ma boundary. Continuing high-resolution analyses of well-dated, shelf-proximal sediments allows scientists to continue piecing together Antarctica's glacial history. In doing so, we improve both our understanding of ice dynamics during past times of great climate change, and our abilities to assess the magnitude of ice response to modern warming.

6. REFERENCES

Anderson, J.B., 1999. *Geologic History of Antarctica.* Antarctic Marine Geology. Cambridge University Press.

Anderson, J.B. et al., 2011. "Progressive Cenozoic cooling and the demise of Antarctica's last refugium". *PNAS.* **108**(28): 11356-11360.

Barker, P.F., Kennett, J.P., et al., 1988. Proceedings of the Ocean Drilling Program, Initial Reports, 113. Ocean Drilling Program, College Station, Texas.

Boggs, Jr, S., 2011. "Principles of Sedimentology and Stratigraphy". 5th edition., Pearson.

Böning, P. et al., 2005. "Geochemical characteristics of Chilean upwelling sediments at ~36°S". *Marine Geology.* **220**(1-4):1-21.

Busetti, M. et al., 2000. "Geological Structure of the South Orkney Microcontinent". *Terra Antarctica.* **8**(2): 71-78.

Carter, A. et al., 2016. "Widespread Antarctic glaciation during the Late Eocene". *Earth and Planetary Science Letters.* **458**(2017):49-57.

Castillo, P. et al., 2014. "Petrography and geochemistry of the Carboniferous-Triassic Trinity Peninsula Group, West Antarctica: implications for provenance and tectonic setting". *Geological Magazine.* **152**(4):575-588.

Cowan, E.A. et al., 2008. "Coarse-grained terrigenous sediment deposition on continental rise drifts: A record of Plio-Pleistocene glaciation on the Antarctic Peninsula". *Palaeogeography, Palaeoclimatology, Palaeoecology.* **265**(3-4): 275-291.

Coxall, H. et al., 2005. "Rapid stepwise onset of Antarctic glaciation and deeper calcite compensation in the Pacific Ocean". *Nature.* **433**: 53-57.

Coxall, H. and Wilson, P., 2011. "Early Oligocene glaciation and productivity in the eastern equatorial Pacific: Insights into global carbon cycling". *Paleoceanography and Paleoclimatology.* **26**(2).

DeConto, R.M. and Pollard, D., 2003. "Rapid Cenozoic glaciation of Antarctic induced by declining atmospheric CO2". *Nature.* **421** (6920): 245-249.

Duprat, L.P.A.M., et al., 2016. "Enhanced Southern Ocean marine productivity due to fertilization by giant icebergs". *Nature Geoscience.* **9:** 219-221.

Eagles, G. and Livermore, R.A., 2002. "Opening history of Powell Basin, Antarctic Peninsula". *Marine Geology.* **185**: 195-205.

Feakins, S.J. et al., 2014. "Snapshot of cooling and drying before onset of Antarctic glaciation". *Earth and Planetary Science Letters.* **404**(2014): 154-166.

Fitzgerald, P. A. U. L., 2002. "Tectonics and landscape evolution of the Antarctic plate since the breakup of Gondwana with an emphasis on the West Antarctic Rift

System and the Transantarctic Mountains." *Royal Society of New Zealand Bulletin*. **35**: 453-469.

Floyd, P.A. and Leveridge, B.E., 1987. "Tectonic environment of the Devonian Gramscatho basin, South Cornwall: framework mode and geochemical evidence from turbiditic sandstones". *Journal of the Geological Society, London.* **144**: 531-542.

Francis, J.E. et al., 2008. "100 Million Years of Antarctic Climate Evolution: Evidence from Fossil Plants". *Antarctica: A Keystone in a Changing World.* Proceedings of the 10th International Symposium on Antarctic Earth Sciences. 19-26.

Francis, J.E. et al., 2009. "From Greenhouse to Icehouse – the Eocene/Oligocene in Antarctica". In: *Developments in Earth & Environmental Sciences.* Chapter 8: 309-368. Elsevier B.V.

Galeotti, S. et al., 2016. "Antarctic Ice Sheet variability across the Eocene-Oligocene boundary climate transition". *Science.* **354**(6281):76-80.

Gromet, L.P. et al., 1984. "The 'North American Shale Composite': Its compilation, major and trace element characteristics". *Geochimica et Cosmochimica Acta.* **48**: 2469-2482.

Grützner, J., 2003. Data report: Multisensor core logging data, coarse-fraction grain-size analyses, and biogenic silica content of upper Miocene-lower Pliocene sediments, ODP Site 1165. *In* Cooper, A.K., O'Brien, P.E., and Richter, C. (Eds.), *Proc. ODP, Sci. Results,* **188.**

Gulick, S.P.S. et al., 2017. "Initiation and long-term instability of the East Antarctic Ice Sheet". *Nature.* **552**: 225-229.

Hebbeln, D., 2000. "Flux of ice-rafted detritus from sea ice in the Fram Strait". *Deep-Sea Research.* **47**: 1773-1790.

Houben, A.J.P. et al., 2011. "*Malvinia escutiana,* a new biostratigraphically important Oligocene dinoflagellate cyst from the Southern Ocean". *Review of Palaeobotany and Palynology.* **165**: 175-182.

Houben, A.J.P. et al., 2012. "The Eocene-Oligocene transition: Changes in sea level, temperature or both?". *Palaeogeography, Palaeoclimatology, Palaeoecology.* **335**: 75-83.

Houben, A.J.P. et al., 2013. "Reorganization of Southern Ocean Plankton Ecosystem at the Onset of Antarctic Glaciation". *Science.* **340**: 341-344.

Huang, X. et al., 2014. "Variability in Cenozoic sedimentation and paleo-water depths of the Weddell Sea basin related to pre-glacial and glacial conditions of Antarctica". *Global and Planetary Change.* **118:** 25-41.

Ivany, L.C. et al., 2006. "Evidence for an earliest Oligocene ice sheet on the Antarctic Peninsula". *Geology.* **34**(5): 377-380.

Katz, M.E. et al., 2008. "Stepwise transition from the Eocene greenhouse to the Oligocene icehouse". *Nature Geoscience.* **1**:329-332.

King, E.C. and Barker, P.F., 1988. "The margins of the South Orkney Microcontinent". *Journal of the Geological Society.* **145**(2): 317-331.

Konert, M. and Vandenberghe, J., 1997. "Comparison of laser grain size analysis with pipette and sieve analysis: a solution for the underestimation of the clay fraction". *Sedimentology.* **44**(3): 523-535.

Krissek, L.A., 1998. "Data Report: Mass Accumulation Rates and Composition of Neogene Ice-Rafted Debris, Site 919, Irminger Basin". *Proceedings of the Ocean Drilling Program, Scientific Results.* **163**: 157-161.

Lear, C.H., et al., 2008. "Cooling and ice growth across the Eocene-Oligocene transition". *Geology.* **36**: 251-254.

Lee, H.M. et al., 2012. "The A-type Pirrit Hills Granite, West Antarctica: an example of magmatism associated with the Mesozoic break-up of the Gondwana supercontinent". *Geosciences Journal.* **16**(4): 421-433.

Light, J., 2017. "Geochemical and Particle Size Analysis of East Antarctic shelf sediments through the Eocene Oligocene Transition". Montclair: Montclair State University.

Livermore, R. et al., 2005. "Paleogene opening of Drake Passage". *Earth and Planetary Science Letters.* **236**: 459-470.

Ma, L. et al., 2011. "Geochemical behaviors of different element groups during shale weathering at the Susquehanna/Shale Hills Critical Zone Observatory". *Applied Geochemistry.* **26**: 589-593.

McLennan, S.M et al., 1993. "Geochemical approaches to sedimentation, provenance, and tectonics". *Geological Society of America: Special Paper.* **284**: 21-40.

McLennan, S.M., 2001. "Relationships between the trace element composition of sedimentary rocks and upper continental crust". *Geochemistry Geophysics Geosystems.* **2**: paper number 2000GC000109.

Middelburg, J.J., 1988. "Chemical processes affecting the mobility of major, minor, and trace elements during weathering of granitic rocks". *Chemical Geology.* **68:** 253-273.

Miller, K.G. et al., 2009. "Climate threshold at the Eocene-Oligocene transition: Antarctic ice sheet influence on ocean circulation". *The Geological Society of America Special Paper.* **452**: 169-178.

Misra, K.C., 2012. "Introduction to Geochemistry: Principles and Applications, First Edition". Blackwell Publishing Ltd.

"Moisture and Density". Janus Data (Exp. 1-312). *International Ocean Discovery Program.*

Murray, R.W. et al., 2000. "Analysis of major and trace elements in rocks, sediments, and interstitial waters by inductively coupled plasma-atomic emission spectrometry (ICP-AES)". *ODP Technical Note, 29.*

Naish, T., 2017. "What does the United Nations Paris Climate Agreement Mean for Antarctica?: Implications for New Zealand's future research priorities". *Antarctic: The Publication of the New Zealand Antarctic Society.* **35**(4): 46-51.

Nakamura, N., 1974. "Determination of REE, Ba, Fe, Mg, Na and K in carbonaceous and ordinary chondrites". *Geochimica et Cosmochimica Acta.* **38**(5): 757-775.

Nesbitt, W. and G.M. Young, 1982. "Early Proterozoic Climates and Plate Motions Inferred from Major Element Chemistry of Lutites". *Nature.* **299**(9885): 715-717.

Pagani, M. et al., 2005. "Marked Decline in Atmospheric Carbon Dioxide Concentrations During the Paleogene". *Science.* **309**(5734): 600-603.

Pälike, H. et al., 2006. "The Heartbeat of the Oligocene Climate System". *Science.* **314**(5807): 1894-1898.

Passchier, S., 2011. "Linkages between East Antarctic Ice Sheet extent and Southern Ocean temperatures based on a Pliocene high-resolution record of ice-rafted debris off Prydz Bay, East Antarctica". *Paleoceanography and Paleoclimatology.* **26**(4): 1-13.

Passchier, S. et al., 2017. "An Antarctic stratigraphic record of stepwise ice growth through the Eocene-Oligocene transition". *Bulletin of the Geological Society of America.* **129**(3-4): 318-330.

Passchier, S. et al., 2018. "Sedimentary processes and facies on a high-latitude passive continental margin, Wilkes Land, East Antarctica". *Glaciated Margins: The Sedimentary and Geophysical Archive.* The Geological Society of London. **475:** 1-21.

Paulsson, O. and Austrheim, H., 2003. "A geochronological and geochemical study of rocks from Gjelsvikfjella, Dronning Maud Land, Antarctica – implications for Mesoproterozoic correlations and assembly of Gondwana". *Precambrian Research.* **125**: 113-138.

Pearce, J A., 1983. Role of the sub-continental lithosphere in magma genesis at active continental margins. In C.J Hawkesworth and M.J. Norry, Eds., Continental basalts and mantle xenoliths. Shiva, Orpington (London), and Birkhauser Boston, Cambridge, Massachusetts.

Pearson, P.N. et al., 2009. "Atmospheric carbon dioxide through the Eocene-Oligocene climate transition". *Nature.* **461**: 1110-1113.

Piper, D.Z. and Bau, M., 2013. "Normalized Rare Earth Elements in Water, Sediments, and Wine: Identifying Sources and Environmental Redox Conditions". *American Journal of Analytical Chemistry.* **4**: 69-83.

Potter, P.E., Maynard, J.B., & Depetris, P.J. Mud and mudstones: Introduction and overview. Springer Science & Business Media, 2005.

Robert, C. and Maillot, H., 1990. "Paleoenvironments in the Weddell Sea area and Antarctic climates, as deduced from clay mineral associations and geochemical data, ODP Leg 113". In *Proceedings of the Ocean Drilling Program, Scientific Results, Vol. 113*. 51-70.

Rose, K.C. et al., 2013. "Early East Antarctic Ice Sheet growth recorded in the landscape of the Gamburtsev Subglacial Mountains". *Earth and Planetary Science Letters.* **375**: 1-12.

Sheldon, N.D. and Tabor, N.J., 2009. "Quantitative paleoenvironmental and paleoclimatic reconstruction using paleosols". *Earth-Science Reviews.* **95:** 1-52.

Sperazza, M. et al., 2004. "High-resolution particle size analysis of naturally occurring very fine-grained sediment through laser diffractometry". *Journal of Sedimentary Research.* **74**(5): 345-370.

Stocchi, P. et al., 2013. "Relative sea-level rise around East Antarctica during Oligocene glaciation". *Nature Geoscience.* **6**: 380-384.

Storti, F. and Balsamo, F., 2010. "Particle size distributions by laser diffraction: sensitivity of granular matter strength to analytical operation procedures". *Solid Earth.* **1**: 25-48.

Tamura, A. et al., 2015. "Measurement of whole-rock trace-element composition by flux-free fused glass and LA-ICP-MS: Evaluation of simple and rapid routine work". *Geochemical Journal.* **49**(3): 243-258.

Thiry, M., 2000. "Palaeoclimatic interpretations of clay minerals in marine deposits: an outlook from the continental origin". *Earth-Science Reviews*. **49**(1-4): 201-221.

Vandenberghe, N. et al., 2012. "The Paleogene Period". *The Geologic Time Scale 2012*. By: Felix M. Gradstein. Amsterdam: Elsevier Science. 855-921.

Vennum, W.R. and Rowley, P.D., 1986. "Reconnaissance geochemistry of the Lassiter Coast Intrusive Suite, southern Antarctic Peninsula". *Geological Society of America Bulletin.* **97**: 1521-1533.

Vennum, W.R. and Storey, B.C., 1987. "Petrology, geochemistry, and tectonic setting of granitic rocks from the Ellsworth-Whitmore Mountains crustal block and Thiel Mountains, West Antarctica". *Geophysical Monograph Series: Structure, Tectonics, and Geophysics.* Published by the American Geophysical Union. **40:** 139-150.

Wang, C. et al., 2013. "The Eocene-Oligocene climate transition in the Tarim Basin, Northwest China: Evidence from clay mineralogy". *Applied Clay Science.* **74**:10-19.

Wedepohl, K.H., 1985. "The composition of the continental crust". *Geochimica et Cosmochimica Acta.* **59**(7): 1217-1232.

Wei, W. and Wise, S.W., 1990. "Middle Eocene to Pleistocene calcareous nanofossil recovered by Ocean Drilling Program Leg 113 in the Weddell Sea. Proc. ODP, Init. Rep., 113: 639-666.

Wentworth, C.K., 1922. "A scale of grade and class terms for clastic sediments". *United States Geological Survey.* Hosted by: University of Chicago Press Journals. 377-392.

Will, T.M. et al., 2010. "Geochemical and isotopic constraints on the tectonic and crustal evolution of the Sheckleton Range, East Antarctica, and correlation with other Gondwana crustal segments". *Precambrian Research.* **180**: 85-112.

Williams, T. et al., 2010. "Evidence for iceberg armadas from East Antarctica in the Southern Ocean during the late Miocene and early Pliocene". *Earth and Planetary Science Letters.* **290**(3-4): 351-361.

Wilson, D.S. et al., 2012. "Antarctic topography at the Eocene-Oligocene boundary". *Palaeogeography, Palaeoclimatology, Palaeoecology.* **335**: 24-34.

Zachos, J., et al., 2001. "Trends, Rhythms, and Aberrations in Global Climate 65 Ma to Present". *Science.* **292***:* 686-692.

7. APPENDIX

Figure A.1 55R major element data by section normalized to NASC values (Gromet et al., 1984). Samples show consistent CaO, MnO, and MgO depletions as well as and Na$_2$O enrichment against NASC concentrations. Slight enrichments and depletions in Fe$_2$O$_3$ are common throughout.
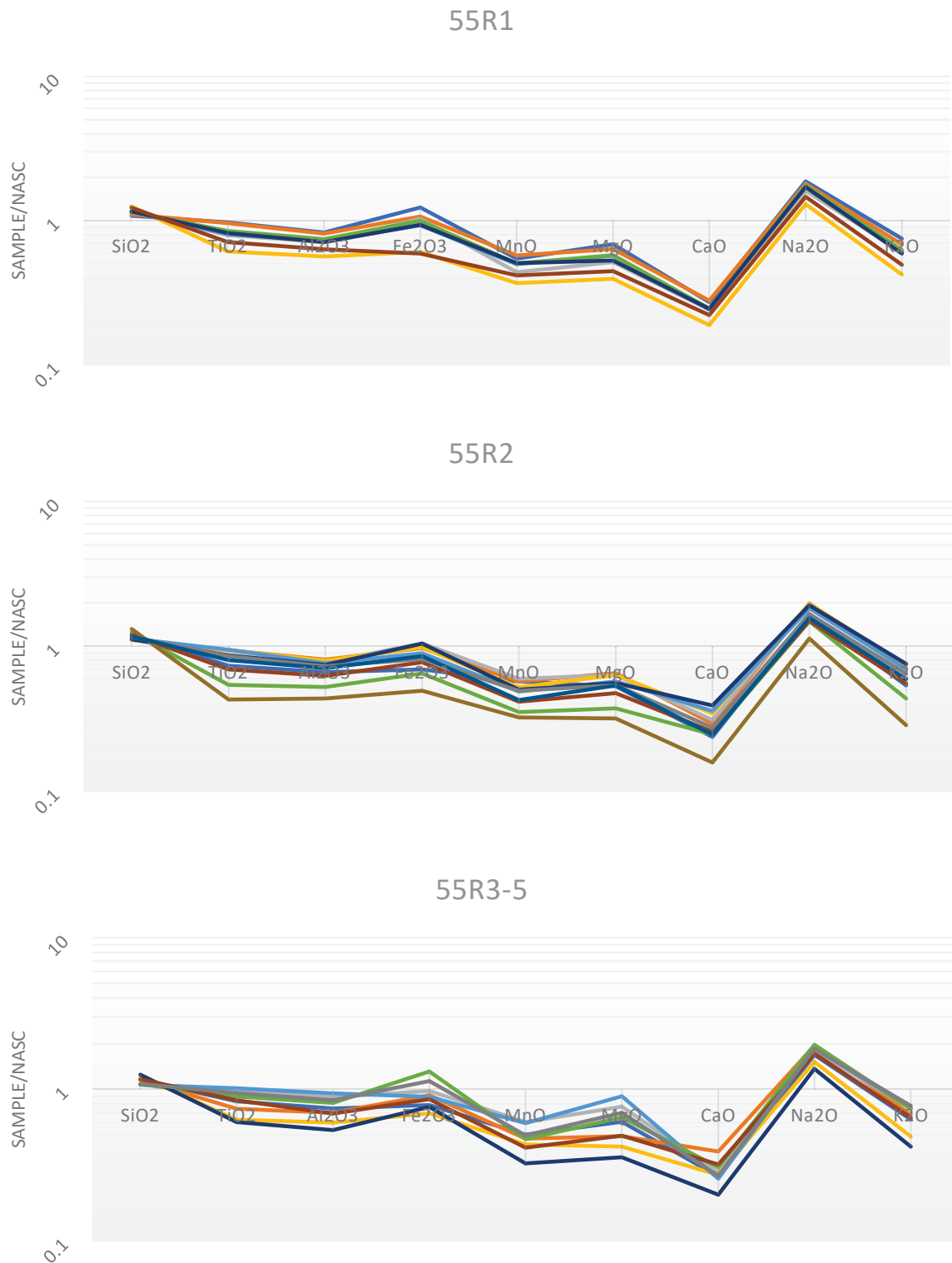
Table A.1. Complete list of samples with corresponding particle size percentages, ages, and depth.
* denotes data from J. Light (2017).

SAMPLE ID	CLAY %	SILT %	SAND %	AGE (Ma)	MBSF
55R1 50-52 cm	30.69	65.28	4.03	33.52	568.7
55R1 55-57 cm	22.55	70.52	6.93	33.53	568.75
55R1 60-62 cm	28	66.18	5.82	33.54	568.8
55R1 65-67 cm	19.36	76.23	4.4	33.55	568.85
55R1 * 70-72 cm	25.6	70.03	4.37	33.56	568.9
55R1 75-77 cm	29.4	66.37	4.24	33.57	568.95
55R1 80-83 cm	17.05	77.15	5.8	33.58	569
55R1 85-88 cm	13.34	40.73	45.93	33.59	569.05
55R1 90-93 cm	22.13	74.35	3.53	33.6	569.1
55R1 94-97cm	15.1	67.04	17.86	33.61	569.15
55R1 100-102 cm	16.37	77.41	6.22	33.62	569.2
55R1 105-107 cm	18.25	79.86	1.89	33.63	569.25
55R1 110-112 cm	16.87	71.13	12	33.64	569.3
55R1 115-118 cm	20.88	75.94	3.18	33.65	569.35
55R1 120-122 cm	14.37	71.82	13.8	33.66	569.4
55R1 125-127 cm	18.76	75.9	5.34	33.67	569.45
55R1 130-132 cm	21.94	75.56	2.5	33.68	569.5
55R1 135-138 cm	18.67	70.8	10.54	33.69	569.55
55R1 145-147 cm	10.26	58.54	31.2	33.71	569.65
55R2 0-2 cm	16.19	74.09	9.72	33.72	569.7

55R2 5-8 cm	17.42	79.31	3.28	33.73	569.75
55R2 10-12 cm	5.4	44.69	49.91	33.74	569.8
55R2 15-17 cm	26.18	69.53	4.29	33.75	569.85
55R2 20-22 cm	14.76	81.26	3.98	33.76	569.9
55R2 25-27 cm	19.94	75.11	4.95	33.77	569.95
55R2 30-32 cm	13.83	80.53	5.63	33.78	570
55R2 35-37 cm	28.94	63.67	7.39	33.79	570.05
55R2 40-42 cm	10.34	75.71	13.96	33.8	570.1
55R2 50-52 cm	20.15	50.52	29.33	33.82	570.2
55R2 55-57 cm	9.41	79.34	11.25	33.83	570.25
55R2 60-62 cm	23.48	54.07	22.45	33.84	570.3
55R2 65-67 cm	12.71	69.32	17.97	33.85	570.35
55R2 75-77 cm	22.92	55.26	21.82	33.87	570.45
55R2 80-82 cm	9.54	74.72	15.74	33.88	570.5
55R2 85-87 cm	11.61	69.66	18.73	33.89	570.55
55R2 90-92 cm	10.68	50.48	38.84	33.9	570.6
55R2 95-97 cm	13.5	39.08	47.42	33.91	570.65
55R2 100-102 cm	18.42	51.04	30.54	33.92	570.7
55R2 105-107 cm	23.89	52.49	23.63	33.93	570.75
55R2 110-112 cm	17.96	76.97	5.07	33.94	570.8
55R2 115-117 cm	16.88	73.07	10.05	33.95	570.85
55R2 120-123 cm	12.13	69.78	18.09	33.96	570.9

55R2 125-127 cm	21.20	72.29	6.51	33.97	570.95
55R2 130-133 cm	8.66	58.09	33.26	33.98	571
55R2 134-137 cm	14.21	74.94	10.85	33.99	571.05
55R2 140-143 cm	14.07	80.08	5.85	34	571.1
55R2 145-147 cm	16.91	79.96	3.13	34.01	571.15
55R3 5-7 cm	17.65	78.02	4.33	34.04	571.25
55R3 25-28 cm	20.88	73.9	5.22	34.08	571.45
55R3 35-37 cm	19.25	62.24	18.51	34.09	571.55
55R3 45-47 cm	17.40	46.28	36.33	34.1	571.65
55R3 55-57 cm	20.97	73.4	5.63	34.11	571.75
55R3 65-67 cm	24.29	70.6	5.11	34.12	571.85
55R3 90-92 cm	16.48	66.1	17.42	34.13	572.1
55R3 110-112 cm	25.94	68.9	5.16	34.14	572.3
55R3 135-137 cm	15.95	66.27	17.78	34.15	572.55
55R4 5-7 cm	20.80	63.08	16.11	34.16	572.75
55R4 25-27 cm	17.41	63.35	19.25	34.17	572.95
55R4 35-37 cm	13.88	54.1	32.02	34.175	573.05
55R4 45-47 cm	19.77	56.32	23.91	34.18	573.15
55R4 56-59 cm	15.03	45.98	38.99	34.185	573.25
55R4 65-67 cm	13.18	61.88	24.95	34.19	573.35
55R4 75-77 cm	21.14	62.03	16.83	34.195	573.45
55R4 90-92 cm	17.76	77.52	4.72	34.2	573.6

55R4 110-112 cm	20.89	61.49	17.63	34.21	573.9
55R4 128-130 cm	15.42	75.35	9.23	34.22	574.2
55R5 5-7 cm	15.21	71.8	12.99	34.23	574.25
55R5 10-12 cm	11.02	59.52	29.46	34.235	574.3
55R5 25-27 cm	15.82	72.75	11.43	34.24	574.45
55R5 45-48 cm	15.83	76.96	7.21	34.25	574.65
55R5 55-57 cm	14.11	69.46	16.43	34.255	574.75
55R5 80-82 cm	16.37	66.09	17.54	34.27	575
55R5 100-103 cm	8.52	65.63	25.85	34.28	575.2
55R5 135-137 cm	23.86	62.38	13.76	34.29	575.55
55R5 140-142 cm	22.40	65.73	11.88	34.295	575.6

Table A.2. List of samples that received modified or adjusted preparation for laser particle size analysis.

SAMPLE ID	NaOH BATH (Y/N)	SONICATION (minutes)
55R1 85-88 cm	N	60
55R1 90-93 cm	Y	30
55R2 5-8 cm	Y	15
55R2 134-137 cm	Y	15
55R2 145-147 cm	Y	30
55R5 100-102 cm	N	30

Table A.3. a) through c) give 55R trace element data (ppm) by section. Averaged from total of four instrument runs, except Co^, which shows results from one run.

a)

55R1 Sample ID	Sc	V	Cr	Co^	Ni	Rb	Zr	Nb	Cs	Hf	Ta	Pb	Th	U
50-52 cm	13.31	100.54	58.62	9.51	26.61	117.19	168.25	8.80	5.49	4.53	0.69	17.98	10.68	4.23
70-72 cm	13.27	103.71	55.63	9.06	26.56	113.84	144.25	10.40	6.01	4.10	0.79	16.22	11.92	3.48
80-83 cm	11.19	89.16	48.87	7.01	24.58	99.42	122.10	8.65	5.16	3.47	0.67	11.52	10.16	2.48
90-93 cm	8.09	66.60	35.30	7.01	21.15	73.52	90.61	6.18	3.83	2.43	0.50	10.19	6.93	3.41
105-107 cm	12.92	105.62	55.29	9.09	29.44	106.46	131.27	8.58	5.35	3.36	0.66	15.85	9.79	3.36
110-112 cm	11.43	92.47	48.32	8.11	25.98	103.31	133.74	8.73	5.00	3.51	0.69	16.79	10.04	3.55
120-122 cm	10.58	80.44	46.14	7.52	22.11	98.68	109.87	8.61	4.88	3.23	0.67	3.54	9.97	3.55
130-132 cm	8.94	71.88	40.97	7.02	21.98	84.84	114.18	7.82	4.19	3.14	0.59	8.22	8.18	3.05

b)

55R2 Sample ID	Sc	V	Cr	Co^	Ni	Rb	Zr	Nb	Cs	Hf	Ta	Pb	Th	U
5-8 cm	10.09	78.25	44.57	8.28	26.33	91.72	117.23	8.13	4.57	3.19	0.63	5.24	8.99	3.37
20-22 cm	12.97	99.81	58.26	9.51	30.50	119.55	165.78	9.86	5.62	4.42	0.78	3.99	11.47	4.25
30.32 cm	14.99	111.70	67.06	8.67	31.08	129.95	171.87	12.07	5.91	4.59	0.855	9.01	12.39	4.56
40-42 cm	14.34	102.23	72.06	9.24	23.63	122.55	213.94	10.69	5.21	5.83	0.79	9.84	11.38	4.46
55-57 cm	17.06	119.55	88.37	7.42	26.67	122.99	273.38	10.65	5.04	6.67	0.73	12.19	9.85	4.53
65-67 cm	7.55	59.56	38.69	6.48	22.72	60.04	118.00	3.72	2.39	2.94	0.36	5.61	5.97	2.77
85-87 cm	13.71	103.43	74.61	6.87	21.10	115.30	229.36	8.72	4.32	5.97	0.66	8.80	11.27	3.75
110-112 cm	11.18	88.30	56.28	7.13	28.63	90.83	165.69	8.00	4.19	4.21	0.59	9.87	7.91	4.06
120-123 cm	12.31	104.04	57.97	8.14	28.74	109.67	186.04	10.40	5.33	5.03	0.75	6.14	9.78	4.53
134-137 cm	6.22	55.49	28.27	6.26	25.74	52.08	80.86	4.58	2.70	2.07	0.37	3.43	5.22	2.67
140-143 cm	12.35	96.32	53.99	6.75	23.52	108.63	138.00	8.06	5.49	3.65	0.70	10.78	10.00	4.63

c)

55R3-R5 Sample ID	Sc	V	Cr	Co^	Ni	Rb	Zr	Nb	Cs	Hf	Ta	Pb	Th	U
R3 25-28 cm	14.97	105.61	69.76	8.44	31.06	113.47	203.84	9.52	5.39	4.85	0.69	16.95	10.22	4.72
R3 65-67 cm	12.33	86.87	60.96	7.1	25.60	103.76	235.94	8.53	3.80	5.99	0.64	4.75	9.54	3.59
R3 110-112 cm	15.25	115.35	63.09	8.43	31.92	137.54	190.17	12.59	6.62	5.35	0.96	6.82	13.48	5.20
R3 135-137 cm	8.39	62.18	39.70	6.09	18.53	75.60	170.32	5.20	3.26	4.31	0.96	6.42	8.29	2.90
R4 90-92 cm	14.09	107.65	61.15	9.83	30.43	123.26	164.35	11.85	5.63	4.45	0.85	13.68	11.85	4.53
R4 110-112 cm	12.38	88.44	61.79	6.62	20.28	110.41	200.59	10.12	4.72	5.39	0.74	13.57	11.47	3.63
R5 45-48 cm	8.36	60.69	41.76	4.85	20.46	68.35	158.17	5.59	3.04	4.02	0.50	7.25	7.88	3.31
R5 80-82 cm	12.68	86.02	67.07	4.84	15.63	104.04	251.90	8.40	4.13	6.67	0.72	8.12	9.86	3.95
R5 135-137 cm	14.00	99.75	67.41	7.37	22.71	124.56	196.72	10.15	5.66	5.46	0.79	14.26	11.53	4.52

Table A.4. a) through c) give 55R rare earth element concentrations (ppm) by section as averaged from four instrument runs.

a)

55R1 Sample ID	La	Ce	Pr	Nd	Sm	Eu	Gd	Tb	Dy	Ho	Er	Tm	Yb	Lu
50-52 cm	29.78	60.26	6.82	25.96	5.33	1.06	4.58	0.72	2.36	0.85	2.22	0.36	2.27	0.36
70-72 cm	31.55	61.22	7.08	26.88	5.47	0.87	4.76	0.73	4.25	0.86	2.31	0.36	2.83	0.36
80-83 cm	25.17	50.16	5.90	22.30	4.44	0.87	3.84	0.60	3.41	0.69	1.85	0.29	1.90	0.29
90-93 cm	18.67	38.26	4.61	17.14	3.42	0.70	3.20	0.50	2.85	0.57	1.46	0.24	1.50	0.23
105-107 cm	32.91	57.78	6.72	25.55	5.07	0.99	4.52	0.70	4.12	0.85	2.25	0.36	2.22	0.36
110-112 cm	26.35	53.83	6.22	23.29	4.76	0.90	4.16	0.65	3.81	0.78	2.07	0.33	2.09	0.33
120-122 cm	25.39	51.83	6.02	22.38	4.49	0.86	3.93	0.61	3.56	0.72	1.89	0.30	1.95	0.31
130-132 cm	20.49	44.64	5.30	19.65	3.89	0.77	3.53	0.55	3.17	0.64	1.69	0.27	1.72	0.26

b)

55R2 Sample ID	La	Ce	Pr	Nd	Sm	Eu	Gd	Tb	Dy	Ho	Er	Tm	Yb	Lu
5-8 cm	23.09	47.95	5.67	21.02	4.25	0.83	3.79	0.60	3.44	0.68	1.83	0.29	1.75	0.28
20-22 cm	30.94	64.49	7.34	27.90	5.59	1.05	4.74	0.74	4.31	0.87	2.33	0.47	2.35	0.37
30.32 cm	35.25	68.65	8.07	30.51	6.11	1.05	5.13	0.80	4.66	0.95	2.53	0.40	2.62	0.40
40-42 cm	31.12	63.53	7.41	28.26	5.72	1.12	4.75	0.74	4.31	0.86	2.27	0.36	2.34	0.35
55-57 cm	42.67	76.03	8.92	33.82	6.74	1.25	5.80	0.91	5.65	1.18	3.23	0.51	3.16	0.48
65-67 cm	15.94	37.52	4.66	17.70	3.71	0.77	3.52	0.55	3.10	0.60	1.56	0.24	1.48	0.22
85-87 cm	32.47	66.94	7.65	29.16	5.84	1.15	4.86	0.74	4.21	0.83	2.18	0.34	2.21	0.34
110-112 cm	26.38	51.07	6.07	23.08	4.58	0.95	4.18	0.65	3.76	0.76	2.01	0.31	2.01	0.31
120-123 cm	27.42	56.79	6.65	25.09	5.08	0.97	4.38	0.69	4.04	0.82	2.23	0.36	2.27	0.35
134-137 cm	15.14	29.99	3.92	14.24	2.86	0.6	2.90	0.46	2.53	0.52	1.32	0.20	1.27	0.19
140-143 cm	25.59	52.79	6.21	23.37	4.64	0.91	3.98	0.62	3.60	0.72	1.92	0.3	2.00	0.30

c)

55R3 – 55R5 Sample ID	La	Ce	Pr	Nd	Sm	Eu	Gd	Tb	Dy	Ho	Er	Tm	Yb	Lu
R3 25-28 cm	38.81	69.50	8.06	30.11	5.95	1.16	5.25	0.83	5.05	1.07	2.93	0.45	2.84	0.44
R3 65-67 cm	30.00	60.09	7.06	26.99	5.45	1.14	4.58	0.72	4.13	0.84	2.34	0.35	2.22	0.35
R3 110-112 cm	35.00	70.73	8.28	31.25	6.45	1.22	5.29	0.84	4.96	1.02	2.75	0.43	2.76	0.43
R3 135-137 cm	20.84	43.83	5.29	19.72	4.00	0.74	3.55	0.55	3.05	0.63	1.65	0.26	1.71	0.27
R4 90-92 cm	32.92	67.45	7.85	29.83	6.06	1.12	4.95	0.76	4.42	0.89	2.37	0.36	2.36	0.36
R4 110-112 cm	27.48	56.70	6.68	25.16	4.92	0.97	4.12	0.64	3.66	0.72	1.91	0.31	1.98	0.30
R5 45-48 cm	20.89	42.95	5.29	19.64	3.80	0.72	3.40	0.51	2.86	0.57	1.49	0.23	1.47	0.23
R5 80-82 cm	28.25	57.46	6.69	25.08	4.93	0.98	4.20	0.64	3.71	0.76	2.05	0.34	2.19	0.34
R5 135-137 cm	29.96	61.44	7.24	27.08	5.48	1.07	4.50	0.71	4.10	0.81	2.15	0.35	2.26	0.35

Table A.5.a) through c) show 55R major element data in normalized weight percent oxides by section. Values from average of three ICP-OES runs conducted in March, 2018.

a)

55R1 Sample ID	SiO_2	TiO_2	Al_2O_3	Fe_2O_3	MnO	MgO	CaO	Na_2O	K_2O	P_2O_5	Total
50-52 cm	70.03	0.68	14.01	6.98	0.03	1.96	0.99	2.14	2.98	0.21	100.00
70-72 cm	71.70	0.67	13.77	6.04	0.03	1.82	1.01	2.06	2.71	0.19	100.00
80-83 cm	74.77	0.56	11.99	5.82	0.03	1.48	0.88	1.84	2.39	0.25	100.00
90-93 cm	81.37	0.43	9.53	3.43	0.02	1.13	0.68	1.49	1.68	0.23	100.00
105-107 cm	74.92	0.57	12.15	5.25	0.03	1.63	0.88	2.00	2.40	0.17	100.00
110-112 cm	74.03	0.59	12.55	5.65	0.03	1.65	0.89	1.99	2.48	0.14	100.00
120-122 cm	75.20	0.57	12.00	5.31	0.03	1.51	0.89	1.95	2.34	0.19	100.00
130-132 cm	79.52	0.50	10.72	3.34	0.03	1.28	0.80	1.67	1.96	0.18	100.00

b)

55R2 Sample ID	SiO$_2$	TiO$_2$	Al$_2$O$_3$	Fe$_2$O$_3$	MnO	MgO	CaO	Na$_2$O	K$_2$O	P$_2$O$_5$	Total
5-8 cm	77.70	0.52	11.22	3.93	0.34	1.52	0.86	1.91	2.14	0.18	100.00
20-22 cm	71.96	0.66	13.71	5.51	0.03	1.87	1.07	2.26	2.76	0.17	100.00
30.32 cm	72.22	0.66	13.07	5.93	0.04	1.82	1.13	2.24	2.68	0.22	100.00
40-42 cm	71.86	0.66	13.46	5.58	0.03	1.82	1.25	2.24	2.94	0.17	100.00
55-57 cm	73.28	0.66	12.92	5.09	0.03	1.64	1.30	2.09	2.78	0.21	100.00
65-67 cm	81.38	0.38	8.87	3.68	0.02	1.07	0.90	1.70	1.74	0.26	100.00
85-87 cm	72.41	0.61	12.57	5.92	0.03	1.60	1.42	2.19	3.00	0.24	100.00
110-112 cm	78.14	0.48	10.58	4.40	0.03	1.36	0.94	1.71	2.21	0.15	100.00
120-123 cm	75.17	0.60	12.33	4.62	0.03	1.54	1.00	1.91	2.56	0.24	100.00
134-137 cm	85.35	0.30	7.40	2.80	0.02	0.91	0.57	1.29	1.14	0.23	100.00
140-143 cm	75.83	0.56	11.99	4.84	0.03	1.54	0.89	1.79	2.36	0.18	100.00

c)

55R3-R5 Sample ID	SiO$_2$	TiO$_2$	Al$_2$O$_3$	Fe$_2$O$_3$	MnO	MgO	CaO	Na$_2$O	K$_2$O	P$_2$O$_5$	Total
R3 25-28 cm	74.96	0.58	12.61	4.45	0.03	1.74	0.97	1.92	2.51	0.21	100.00
R3 65-67 cm	74.53	0.52	11.83	5.18	0.03	1.40	1.41	2.21	2.70	0.18	100.00
R3 110-112 cm	70.33	0.69	15.03	5.52	0.04	2.19	1.02	2.05	2.96	0.16	100.00
R3 135-137 cm	79.28	0.44	10.18	3.92	0.03	1.19	0.99	1.73	1.94	0.30	100.00
R4 90-92 cm	69.49	0.71	15.91	5.04	0.04	2.57	0.93	2.14	2.97	0.19	100.00
R4 110-112 cm	69.81	0.63	13.74	7.41	0.03	1.87	1.11	2.24	2.96	0.21	100.00
R5 45-48 cm	80.96	0.42	9.09	4.33	0.02	1.02	0.73	1.56	1.66	0.21	100.00
R5 80-82 cm	75.44	0.59	11.70	4.87	0.02	1.41	1.16	1.96	2.58	0.26	100.00
R5 135-137 cm	70.17	0.66	14.30	6.41	0.03	2.00	0.97	2.11	3.09	0.26	100.00